nature medicine

JI WOONG PARK 6/19/18 JOURNAL CLUB

ARTICLES

https://doi.org/10.1038/s41591-018-0005-y

Targeting sphingosine-1-phosphate lyase as an anabolic therapy for bone loss

Sarah Weske[1], Mithila Vaidya[1], Alina Reese[1], Karin von Wnuck Lipinski[1], Petra Keul[1], Julia K Bayer[2], Jens W Fischer[2], Ulrich Flögel[3], Jens Nelsen[4], Matthias Epple[4], Marta Scatena[5], Edzard Schwedhelm[6,7], Marcus Dörr[8,9], Henry Völzke[10], Eileen Moritz[8,11], Anke Hannemann[12], Bernhard H Rauch[8,11], Markus H Gräler[13], Gerd Heusch[1] and Bodo Levkau[1]*

Sphingosine-1-phosphate (S1P) signaling influences bone metabolism, but its therapeutic potential in bone disorders has remained unexplored. We show that raising S1P levels in adult mice through conditionally deleting or pharmacologically inhibiting S1P lyase, the sole enzyme responsible for irreversibly degrading S1P, markedly increased bone formation, mass and strength and substantially decreased white adipose tissue. S1P signaling through $S1P_2$ potently stimulated osteoblastogenesis at the expense of adipogenesis by inversely regulating osterix and PPAR-γ, and it simultaneously inhibited osteoclastogenesis by inducing osteoprotegerin through newly discovered p38–GSK3β–β-catenin and WNT5A–LRP5 pathways. Accordingly, $S1P_2$-deficient mice were osteopenic and obese. In ovariectomy-induced osteopenia, S1P lyase inhibition was as effective as intermittent parathyroid hormone (iPTH) treatment in increasing bone mass and was superior to iPTH in enhancing bone strength. Furthermore, lyase inhibition in mice successfully corrected severe genetic osteoporosis caused by osteoprotegerin deficiency. Human data from 4,091 participants of the SHIP-Trend population-based study revealed a positive association between serum levels of S1P and bone formation markers, but not resorption markers. Furthermore, serum S1P levels were positively associated with serum calcium , negatively with PTH , and curvilinearly with body mass index. Bone stiffness, as determined through quantitative ultrasound, was inversely related to levels of both S1P and the bone formation marker PINP, suggesting that S1P stimulates osteoanabolic activity to counteract decreasing bone quality. S1P-based drugs should be considered as a promising therapeutic avenue for the treatment of osteoporotic diseases.

S1P has fundamental functions in development, immunity, and, as recently recognized, bone metabolism[1,2]. Extracellular S1P signals through $S1P_1$–$S1P_5$, which are G protein–coupled receptors[3]. S1P is synthesized via ceramide deacylation followed by phosphorylation through sphingosine kinase 1 (SPHK1) and SPHK2. Its concentrations in vivo are tightly regulated by dephosphorylation through two S1P-specific phosphatases and three lipid phosphate phosphatases and by irreversible degradation into phosphoethanolamine and 2-hexadecanal through a single enzyme, the S1P lyase[4].

Bone is a dynamically regulated tissue undergoing continuous remodeling by the coordinated action of osteoclasts (OCs) and osteoblasts (OBs)[5]. The contribution of S1P to bone homeostasis has been attributed mainly to bone remodeling with particular emphasis on its alleged role in regulating the circulation of OC progenitors (OPs)[6–8]. It has been postulated that an assumed but unproven S1P gradient between bone and plasma chemoattracts OPs away from bone through $S1P_1$, while simultaneously chemorepulsing them through $S1P_2$, with opposite consequences for osteoclastogenesis[9,10]. However, there is little insight into how these mechanisms interact or what their net effect on bone mass may be, particularly as both $S1P_1$ and $S1P_2$ have the same equilibrium dissociation constant (K_D) for S1P. On the other hand, numerous studies have shown that S1P alters OB behavior: (i) OC-secreted S1P stimulates receptor activator of NF-κβ ligand (RANKL) production in OBs[8] and promotes OB differentiation[11]; (ii) cathepsin K deletion in OCs increases bone formation by stimulating SPHK1 activity[12] and (iii) calcitonin stimulates OBs through S1P3 by controlling S1P export in OCs[7].

These observations imply that S1P is an important factor in the functional coupling between OCs and OBs, although the involved mechanisms and especially their relevance in normal and diseased bone homeostasis remain unclear. This is of particular interest if S1P-based drugs are to be considered as a therapeutic option for bone disorders. Specifically, the effects of any deliberate alteration of S1P concentrations on bone metabolism in vivo are unknown. The only insight comes from a 'high turnover' bone phenotype described for newborn mice with global S1P lyase deficiency, although early death at only 2 to 3 weeks of age[7,13] in these mice limits their relevance for studies in adult bone physiology.

[1]Institute for Pathophysiology, West German Heart and Vascular Center, University Hospital Essen, University of Duisburg-Essen, Essen, Germany. [2]Institute of Pharmacology and Clinical Pharmacology, University of Düsseldorf, Düsseldorf, Germany. [3]Institute of Molecular Cardiology, University of Düsseldorf, Düsseldorf, Germany. [4]Institute of Inorganic Chemistry, University of Duisburg-Essen, Essen, Germany. [5]Department of Bioengineering, University of Washington, Seattle, WA, USA. [6]Institute of Clinical Pharmacology and Toxicology, University Medical Center Hamburg-Eppendorf, Hamburg, Germany. [7]German Centre for Cardiovascular Research (DZHK), partner site Hamburg, Hamburg, Germany. [8]DZHK, partner site Greifswald, Greifswald, Germany. [9]Department of Internal Medicine B, University Medicine Greifswald, Greifswald, Germany. [10]Institute for Community Medicine, University Medicine Greifswald, Greifswald, Germany. [11]Institute of Pharmacology, Department of General Pharmacology, University Medicine Greifswald, Greifswald, Germany. [12]Institute of Clinical Chemistry and Laboratory Medicine, University Medicine Greifswald, Greifswald, Germany. [13]Department of Anesthesiology and Intensive Care Medicine, Center for Sepsis Control and Care, and Center for Molecular Biomedicine, University Hospital Jena, Jena, Germany. *e-mail: bodo.levkau@uni-due.de

In this study, we have addressed the question of whether altering S1P levels and gradients in adult mice affected bone homeostasis and quality. Using genetic and pharmacological means to inhibit S1P degradation, we have discovered pronounced osteoanabolic and antiresorptive effects of S1P that are dependent on S1P receptor signaling and, surprisingly, are accompanied by profound alterations in adipose tissue homeostasis. We have identified several nonredundant mechanisms underlying these effects and show that manipulating S1P receptor signaling shifts the balance between bone and adipose tissue with clear therapeutic benefits in preclinical models of genetic and hormonal osteoporosis. Accordingly, we have found strong associations between S1P and bone quality in the 4,091 participants of a large German population-based study, widely implicating S1P in bone health and urging the exploitation of S1P-based therapies in human osteoporosis.

Results

Deletion or inhibition of S1P lyase increases bone mass and strength, raises osteoprotegerin and suppresses OCs. To determine whether elevation of S1P concentrations in vivo affected bone homeostasis in adult mice, we deleted S1P lyase (*Sgpl1*) after complete skeletal remodeling in inducible S1P lyase–knockout mice, in which expression of Cre recombinase is driven by an inducible β-actin promoter (ACTB-CreERT2), yielding *Sgpl1*$^{flox/flox}$ Cre^{+} (KO) mice and *Sgpl1*$^{flox/flox}$ Cre^{-} (control) littermates[14]. Eight months after induction, micro-CT (μCT) analysis of long bones revealed that femoral trabecular bone volume/tissue volume (BV/TV) was 4.5-fold higher, trabecular number (Tb.N.) was 3.7-fold higher and trabecular separation (Tb.Sp.) was 27% lower in KO mice than in control mice of identical age and sex (Fig. 1a). Trabecular thickness (Tb.Th.) was not different between groups (Fig. 1a).

The high bone mass phenotype was reproduced in adult C57BL/6J mice through pharmacological S1P lyase inhibition using 4-deoxypyrodoxin (DOP) for 12 weeks: as determined through μCT and confirmed with quantitative histomorphometry, BV/TV and Tb.N. were 1.3-fold and 1.7-fold higher, respectively, and Tb.Sp. was 24% lower in DOP-treated mice than in age- and sex-matched controls (Fig. 1b and Supplementary Fig. 1). Notably, both trabecular and cortical bone mass were clearly increased in DOP-treated mice, as revealed by μCT analysis of cortical thickness (Ct.Th.) at the femoral midshaft (Fig. 1c); bone mineral density (BMD) was also higher by an impressive 28% (Fig. 1c). The direct consequence of such changes was a greatly improved mechanical bone strength, as assessed in a three-point bending test of the femur (Fig. 1d). Of all parameters measured, ultimate force was higher and elastic modulus was lower in DOP-treated mice than in controls, whereas stiffness and ultimate stress remained the same between groups (Fig. 1d). Elastic modulus and ultimate stress were also lower in the inducible KO mice than in controls, whereas other parameters were unaffected (Supplementary Fig. 2a).

FTY720 (fingolimod) is an S1P analog that, after phosphorylation, acts on four of the five S1P receptors (except the $S1P_2$ receptor) and is approved for treatment of relapsing multiple sclerosis[15]. To test its effect on bone formation and gain insight into the possible S1P receptors involved, we treated adult mice with FTY720 (1.25 mg per kg body weight per day) for 7 weeks. FTY720 had no effect on any bone parameter (Supplementary Fig. 2b) despite inducing the expected lymphopenia, suggesting that perhaps $S1P_2$ was mediating the effect of S1P on bone.

To understand the involved mechanisms, we assessed OB and OC activity status in bones of DOP-treated mice through analyzing dynamic bone formation and staining for osteoid and tartrate resistant acid phosphatase (TRAP). We observed a 23% higher mineral apposition rate (MAR), no changes in bone formation rate (BFR/BS) and a 28% lower osteoid surface per bone surface (OS/BS) in DOP-treated mice compared to controls (Fig. 1e). These data suggested enhanced osteoid mineralization. In respect to OC status, we observed a 48% lower number of TRAP^{+} OCs in DOP-treated mice compared to untreated controls as determined through histomorphometric analysis of OC surface/bone surface (OC.S./B.S.) ratio (Fig. 1f).The plasma concentration of pyridinoline cross-links (PYD), a measure of OC activity in vivo, was reduced by 56% in DOP-treated mice relative to untreated controls (Fig. 1g). To address the mechanisms underlying suppressed OC activity, we analyzed the osteoprotegerin (OPG)–RANKL system as a crucial determinant of OC differentiation and activity[16]. We observed that plasma OPG concentrations were clearly elevated in both inducible KO (1.4-fold) and DOP-treated mice (2.8-fold) compared to their respective controls (Fig. 1h,i). Plasma RANKL concentrations were 96% lower in these groups, and the RANKL/OPG ratio was reduced by 99% (Fig. 1i,j). Again, FTY720 treatment had no effect on any parameter (Supplementary Fig. 2c).

S1P and $S1P_2$ induce OPG through p38–GSK3β–β-catenin and noncanonical WNT5A–LRP5 signaling. To investigate the molecular mechanisms underlying the increased OPG concentrations in plasma, which cause OC inhibition following S1P lyase deletion or inhibition in vivo, we directly tested the effect of S1P on OB progenitors and primary OBs in vitro. Stimulation of MC3T3-E1 cells with S1P for 24 h resulted in a 2.5-fold increase of OPG secretion into the culture medium compared to untreated MC3T3-E1 cells (Fig. 2a). This was preceded by 5.5-fold induction of *Tnfrsf11b* (*Opg*) gene expression 6 h after S1P stimulation (Fig. 2a). In MC3T3-E1 cells, preincubation with the selective $S1P_2$ inhibitor JTE-013 completely abolished the effect of S1P on OPG production, whereas the $S1P_3$ inhibitor TY52156 had no effect (Fig. 2a). These findings were corroborated in primary OBs from wild-type mice, in which stimulation with S1P for 24 h increased OPG protein release into the culture medium by 1.8-fold; this process was completely blocked by JTE013 (Fig. 2b). Furthermore, S1P increased *Opg* gene expression in these cells by 5.5-fold (Fig. 2b). To validate the JTE013 data using genetic means, we stimulated OBs from *S1p2*$^{-/-}$ mice with S1P and observed that they failed to respond with an increase in *Opg* expression (Fig. 2b). This clearly identified $S1P_2$ as the S1P receptor responsible for OPG production.

Opg gene expression is under transcriptional control of the β-catenin–TCF1 pathway[17], prompting us to investigate what effect $S1P_2$ has on it. Stimulation of MC3T3-E1 cells with S1P for 4 h resulted in substantial nuclear accumulation of β-catenin that was abolished by JTE013 (Fig. 2c). Accordingly, stimulation with S1P for 5 and 10 min resulted in increased phosphorylation of glycogen synthase kinase 3β (GSK3β) at the Ser9 residue (Fig. 2d). Notably, GSK3β^{Ser9} phosphorylation did not result from concomitant Akt activation, as JTE013 prevented GSK3β^{Ser9} phosphorylation but not phosphorylation of Akt at Ser473 by S1P (Fig. 2d), suggesting that other kinases were responsible. Activation of canonical Wnt–β-catenin signaling, among other pathways, has been shown to induce GSK3β^{Ser9} phosphorylation[18], whereas WNT3A-mediated activation of p38MAPK phosphorylates the same residue in GSK3β, which stimulates β-catenin–TCF1 transcription[19]. Thus, we tested whether S1P enhanced p38MAPK phosphorylation. Indeed, this was the case, and JTE013 completely abolished this phosphorylation (Fig. 2d). Most importantly, the p38MAPK inhibitor SB203580 abrogated both GSK3β phosphorylation and OPG secretion induced by S1P (Fig. 2e,f).

We next examined whether Wnt family members are regulated by S1P and whether they contribute to OPG stimulation, as canonical Wnt signaling, and specifically WNT5A, have been shown to upregulate *TNFRSF11B* (*OPG*) gene expression in human osteoblastic cells[20]. Real-time PCR analysis of primary OBs revealed that *Wnt5a* gene expression, but not that of *Wnt3a* or *Wnt10b*, was induced 2.9-fold by S1P compared to untreated cells (Fig. 2g).

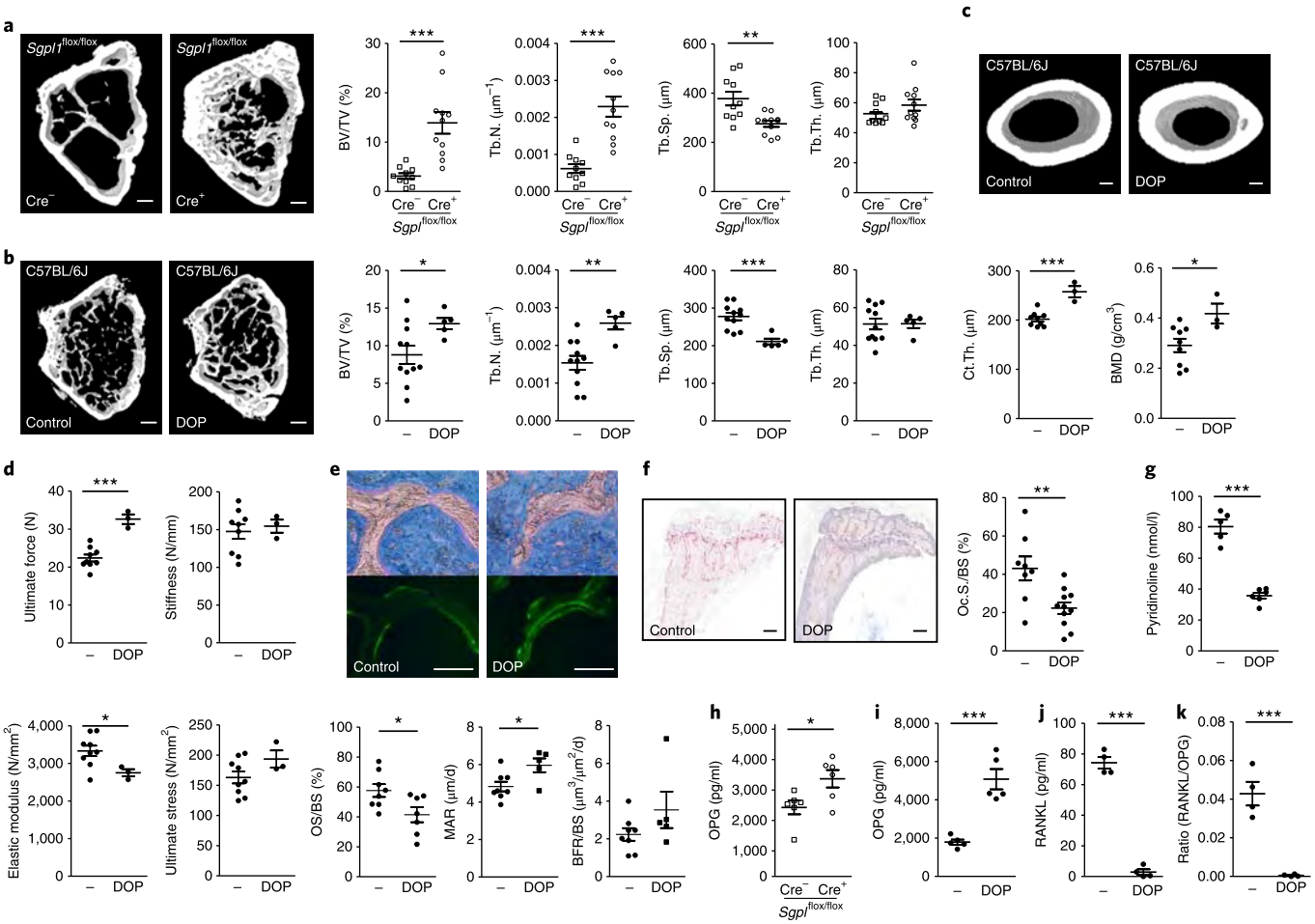

Fig. 1 | Deficiency or inhibition of S1P lyase results in higher bone mass and strength, altered OC activity and increased plasma OPG. a, μCT analysis of the spongiosa of the femoral metaphysis of *Sgpl*$^{flox/flox}$ Cre^{+} and *Sgpl*$^{flox/flox}$ Cre^{-} mice (65 weeks of age, $n=10$ Cre^{-} mice, 11 Cre^{+} mice). Representative images (left) and quantification of trabecular BV/TV, Tb.N., Tb.Sp. and Tb.Th. (right) are shown. Scale bars, 350 μm. **b**, μCT analysis of the femoral metaphysis of 23-week-old male C57BL/6 J mice after 12 weeks of DOP treatment ($n=5$ DOP-treated mice, 11 untreated controls). Representative images (left) and quantification of trabecular BV/TV, Tb.N., Tb.Sp. and Tb.Th. (right) are shown. Scale bars, 350 μm. **c**, Top, μCT analysis of the corticalis at the femoral midshaft of 23-week-old male C57BL/6 J mice after 12 weeks of DOP treatment ($n=3$ DOP-treated mice, 9 untreated controls). Bottom, quantification of Ct.Th. and BMD in these mice. Scale bars, 200 μm. **d**, Ultimate force, stiffness, elastic modulus and ultimate stress as assessed through three-point bending tests of femoral midshafts after 12 weeks of DOP treatment ($n=3$ DOP-treated mice, 9 untreated controls). **e**, Top, tetrachrome staining and calcein dual labeling of tibiae. Bottom, histomorphometric analysis of OS/BS, MAR and BFR/BS (32-week-old mice; at least $n=5$ DOP-treated mice, 8 untreated controls for each individual parameter). Scale bars, 80 μm. **f**, Left, TRAP staining of tibiae and histomorphometric analysis. Right, quantification of OC.S./B.S. ratio (32-week-old mice; $n=11$ DOP-treated mice, 8 untreated controls). Scale bars, 200 μm. **g**, Concentration of pyridinoline cross-links in plasma after 8 weeks of DOP ($n=6$ DOP-treated mice, 5 untreated controls). **h**,**i**, OPG plasma concentration in *Sgpl*$^{flox/flox}$ Cre^{-} and *Sgpl*$^{flox/flox}$ Cre^{+} mice (**h**; $n=6$ Cre^{+} mice, 6 Cre^{-} mice; **h**) and C57BL/6 J mice after 6 weeks of DOP treatment (**i**; $n=5$ mice per group). **j**, RANKL plasma concentration after 6 weeks of DOP ($n=4$ mice per group). **k**, RANKL/OPG ratio in plasma after 6 weeks of DOP ($n=4$ mice per group). Data are presented as mean ± s.e.m. A two-tailed *t*-test was used for statistical analysis. $^{*}P<0.05$; $^{**}P<0.01$; $^{***}P<0.001$.

In addition, expression of the Wnt receptor low-density lipoprotein receptor–related protein 5 (*Lrp5*) was also increased 1.8-fold by S1P (Fig. 2h). Both were abrogated by JTE013 and absent in *S1p2*-deficient OBs (Fig. 2g,h), suggesting an important role for this pathway. Notably, administration of recombinant Wnt inhibitory factor 1 (WIF-1) or the WNT5A-specific inhibitor BOX5 together with S1P clearly suppressed *Opg* gene induction (Fig. 2i).

S1P lyase inhibition rescues *Opg*$^{-/-}$ mice from severe osteoporosis through stimulating OBs. To examine whether the increase in OPG production by S1P was necessary and sufficient for the observed bone mass increase after S1P lyase deletion or inhibition in vivo, we treated adult *Opg*$^{-/-}$ mice suffering from massive osteoporosis[21] with DOP for 8 weeks. To our surprise, we observed a dramatic (30-fold) increase of the almost nonexistent trabecular bone volume of *Opg*$^{-/-}$ mice after DOP treatment, raising their BV/TV to values comparable with those of wild-type controls (Fig. 2j). DOP also increased BV/TV in wild-type controls by ~3-fold as compared to untreated wild-type mice (Fig. 2j). DOP had no effect on Ct.Th. and BMD in *Opg*$^{-/-}$ mice but resulted in a 1.8-fold higher ultimate force in treated versus untreated *Opg*$^{-/-}$ mice (Fig. 2k and Supplementary Fig. 3a). The RANKL plasma concentration was already 16-fold higher in *Opg*$^{-/-}$ mice than in wild-type controls and was not altered by DOP (Fig. 2l), although TRAP-positive area per bone area was reduced by 69% in DOP-treated versus untreated *Opg*$^{-/-}$ mice (Fig. 2m).

As S1P lyase inhibition resulted in higher bone mass even in the absence of OPG, we searched for OPG-independent, OB-dependent

mechanisms. DOP treatment led to a reduction of OS/BS in *Opg*$^{-/-}$ mice (Supplementary Fig. 3b) very similar to that seen in DOP-treated C57BL/6J mice (Fig. 1e), suggesting, along with the increase in MAR (Fig. 1e), higher OB activity and mineralization. To address OB activity in vivo, we measured plasma concentrations of procollagen I C-terminal propeptide (PICP), a reliable marker for OB activity in vivo. Interestingly, we observed a clear 40–50% elevation in PICP concentrations following DOP in both *Opg*$^{-/-}$ and wild-type controls (Fig. 2n). We found this to be a general phenomenon, as C57BL/6J mice that were treated with DOP and *Sgpl1*$^{-/-}$ mice also had higher PICP concentrations compared to their respective controls (Fig. 2o,p). Moreover, alkaline phosphatase (ALP) staining of femora of *Sgpl1*$^{-/-}$ mice revealed a 1.55-fold increase compared to controls (Fig. 2q).

S1P and S1P$_2$ control OB differentiation through activating osterix and inhibiting PPAR-γ. The high plasma PICP concentration with S1P lyase inhibition and deficiency and the notion that altered *Opg* expression has often served as an indicator of general changes of OB phenotype[16] led us to investigate genes associated with OB differentiation after S1P stimulation of primary OBs. Notably, expression of the genes encoding periostin, osteocalcin, osteonectin and collagen type I alpha was 3- to 4-fold higher after stimulation with S1P for 6 h (Fig. 3a). In contrast, in OBs from *S1pr2* (*S1p2*)$^{-/-}$ mice, S1P had no effect on the expression levels of any of these genes (Fig. 3a). S1P also increased calcium deposition by twofold in wild-type OBs, and this was 40% lower than the effect of S1P in OBs from *S1p2*$^{-/-}$ mice (Fig. 3b). S1P$_2$-deficient OBs already had impaired calcium deposition (by 50%) under basal conditions (Fig. 3b). S1P also stimulated cell proliferation in a S1P$_2$-dependent manner: treatment with S1P over 6 d resulted in a 1.4-fold higher number of OBs in wild-type mice, but not in *S1p2*$^{-/-}$ mice (Fig. 3c).

The earliest steps of OB differentiation from mesenchymal progenitors require the orchestrated suppression of adipogenic transcription factors, such as PPAR-γ and CCAAT-enhancer-binding protein (C/ebp)-α and activation of the osteoblastogenic transcription factors osterix, Runt-related transcription factor 2 (Runx2) and β-catenin[22–24]. To understand the fundamental changes in OB differentiation with S1P, we assessed their osteoblastogenic and adipogenic transcription factor profile. We observed that S1P potently induced *Sp7* (*Osterix*) gene expression (by 2.4-fold) in OBs from wild-type mice, but this did not occur in *S1p2*$^{-/-}$ mice or in the presence of JTE013 (Fig. 3d and Supplementary Fig. 4a). *Runx2* expression was unaltered (Supplementary Fig. 4b). In contrast, S1P suppressed *Pparg* and *Cebpa* (*C/ebp-alpha*) expression by 40% and 50%, respectively, in OBs from wild-type mice but not those from *S1p2*$^{-/-}$ mice (Fig. 3e,f). Several direct transcriptional target genes of PPAR-γ, such as the *Cd36*, *Cfd* (*Adipsin*), *Fabp4* and *Lpl* (encoding lipoprotein lipase) were clearly downregulated by S1P (Fig. 3g). Moreover, *Pparg* expression was 1.9-fold higher in OBs from *S1p2*$^{-/-}$ mice than in those from wild-type mice under unstimulated conditions (Fig. 3e). To address the functional interaction between S1P and PPAR-γ, we stimulated OBs with the PPAR-γ agonist rosiglitazone together with S1P and observed that this completely abolished the induction of *Postn*, *Bglap* and *Opg* by S1P (Fig. 3h) and the inhibition of *Fabp4* and *Cd36* (Fig. 3i).

PPAR-γ is a major determinant of adipogenesis[25]. This led us to examine whether PPAR-γ inhibition by S1P affected not only preosteoblast but also preadipocyte differentiation. Indeed, treatment of preadipocytic 3T3L1 cells with S1P for 48 h clearly suppressed *Pparg* gene expression and that of the PPAR-γ target genes *Fabp4* and *Lpl* (Fig. 3j). This was mirrored by an inhibitory effect on adipogenesis, as S1P treatment of 3T3L1 cells over 6 d clearly suppressed adipogenic differentiation (Fig. 3k). In line with a role for S1P$_2$, JTE013 abolished the anti-adipogenic effect of S1P and,

Fig. 2 | S1P induces OPG secretion in OBs through S1P$_2$. **a**, Left, OPG secretion by MC3T3-E1 cells that received 24 h of treatment with combinations of S1P, TY52156 and JTE013 (1 μM each) or no treatment ($n = 4$ for all groups, except $n = 5$ untreated controls and 5 treated with only S1P; fold to baseline). Right, *Opg* gene expression in MC3T3-E1 cells that received 6 h of treatment with S1P and/or JTE013 or no treatment ($n = 3$ for all treatment groups, 4 untreated controls; fold to baseline). **b**, Left, OPG secretion by primary OBs from C57BL/6 J mice that received 24 h of treatment with S1P and/or JTE013 in vitro (1 μM each) or no treatment ($n = 4$ untreated control OBs and S1P-treated OBs; $n = 3$ JTE013- and S1P–JTE013-treated OBs; fold to baseline). Right, *Opg* gene expression in OBs from *S1p2*$^{+/+}$ and *S1p2*$^{-/-}$ mice that received 24 h of S1P treatment in vitro (1 μM) or no treatment ($n = 3$ mice per group; fold to baseline). **c**, Representative cropped western blot of nuclear β-catenin in MC3T3-E1 cells treated with S1P and/or JTE013 (1 μM each) or with LiCl as control (1 mM; $n = 3$ western blots per condition). **d**, Representative cropped western blot of phosphorylated GSK3β^{Ser9} (p-GSK3β^{Ser9}), p-Akt^{Ser473}, p-p38MAPK$^{Thr180/Try182}$, GSK3β and p38MAPK in cytosolic extracts of MC3T3-E1 cells that were untreated or treated with S1P and/or JTE013 (1 μM each; $n = 3$ western blots per condition). **e**, Representative cropped western blot of cytosolic extracts of p-GSK3β^{Ser9} in MC3T3-E1 cells that were untreated or treated with S1P (1 μM) and/or SB203580 (10 μM; $n = 3$ western blots per condition). **f**, OPG secretion measured in supernatants of MC3T3-E1 cells that received 24 h of treatment with S1P (1 μM) and/or SB203580 (10 μM) or no treatment ($n = 3$ for all groups; fold to baseline). **g**, *Wnt5a* expression in OBs from *S1p2*$^{+/+}$ and *S1p2*$^{-/-}$ mice that received 24 h of treatment with S1P and/or JTE013 in vitro (1 μM each) or no treatment ($n = 6$ for all groups, except $n = 3$ JTE-treated *S1p2*$^{+/+}$ OBs and $n = 3$ untreated *S1p2*$^{-/-}$ OBs; fold to baseline). **h**, *Lrp5* expression in OBs from *S1p2*$^{+/+}$ and *S1p2*$^{-/-}$ mice that received 24 h of treatment with S1P and/or JTE013 in vitro (1 μM each) or no treatment ($n = 6$ for all groups, except $n = 3$ S1P-treated *S1p2*$^{+/+}$ OBs and $n = 3$ S1P–JTE013-treated OBs; fold to baseline). **i**, OPG secretion by OBs from C57BL/6 J mice that received 24 h of in vitro treatment with S1P (1 μM), WIF-1 (3.5 μg/ml) and/or BOX5 (100 μM) or no treatment ($n = 5$ for all groups, except $n = 4$ OBs treated only with WIF-1 and $n = 4$ OBs treated with S1P and WIF-1; fold to baseline). **j**, μCT analysis of the femoral metaphysis of 16-week-old *Opg*$^{+/+}$ and *Opg*$^{-/-}$ mice that were untreated or treated with DOP for 8 weeks ($n = 13$ untreated *Opg*$^{+/+}$ controls, 9 DOP-treated *Opg*$^{+/+}$ mice and untreated *Opg*$^{-/-}$ controls, 8 DOP-treated *Opg*$^{-/-}$ mice). Scale bars, 350 μm. **k**, Ultimate force as assessed by three-point bending tests of femoral midshafts of *Opg*$^{+/+}$ and *Opg*$^{-/-}$ mice that were untreated or treated with DOP for 8 weeks ($n = 7$ untreated *Opg*$^{+/+}$ controls, 8 DOP-treated *Opg*$^{+/+}$ mice, 6 untreated *Opg*$^{-/-}$ controls, 5 DOP-treated *Opg*$^{-/-}$ mice). **l**, RANKL plasma concentrations of *Opg*$^{+/+}$ and *Opg*$^{-/-}$ mice that were untreated or treated with DOP for 8 weeks ($n = 6$ untreated *Opg*$^{+/+}$ controls, 5 DOP-treated *Opg*$^{+/+}$ mice, 3 untreated *Opg*$^{-/-}$ controls, 3 DOP-treated *Opg*$^{-/-}$ mice). **m**, Histomorphometric analysis of the ratio of TRAP$^+$ area to total bone area in *Opg*$^{-/-}$ mice that were untreated or treated with DOP for 8 weeks ($n = 3$ mice per group). **n**, PICP plasma concentrations in *Opg*$^{+/+}$ and *Opg*$^{-/-}$ mice that were untreated or treated with DOP for 8 weeks. ($n = 7$ untreated *Opg*$^{+/+}$ controls, 5 DOP-treated *Opg*$^{+/+}$ mice, 8 untreated *Opg*$^{-/-}$ controls and DOP-treated *Opg*$^{-/-}$ mice). **o**, PICP plasma concentration in *Sgpl*$^{flox/flox}$ Cre$^-$ and Cre$^+$ mice ($n = 5$ Cre$^-$ mice, 6 Cre$^+$ mice). **p**, PICP plasma concentration in C57BL/6 J mice that were untreated or treated with DOP for 8 weeks ($n = 4$ control mice, 5 DOP-treated mice). **q**, Representative images (left) and quantification (right) of ALP staining in *Sgpl*$^{flox/flox}$ Cre$^-$ and Cre$^+$ mice ($n = 3$ mice per group). Scale bars: left, 200 μm; right, 100 μm. Data are presented as mean ± s.e.m. A one-way ANOVA with Tukey's multiple-comparisons test (**a**–**l**, **n**) and a two-tailed *t*-test (**m**, **o**, **p**, **q**) were used for statistical analysis. $^*P < 0.05$; $^{**}P < 0.01$; $^{***}P < 0.001$; § $P <$ 0.05 compared to untreated controls. Uncropped images of western blots are available in Supplementary Fig. 12.

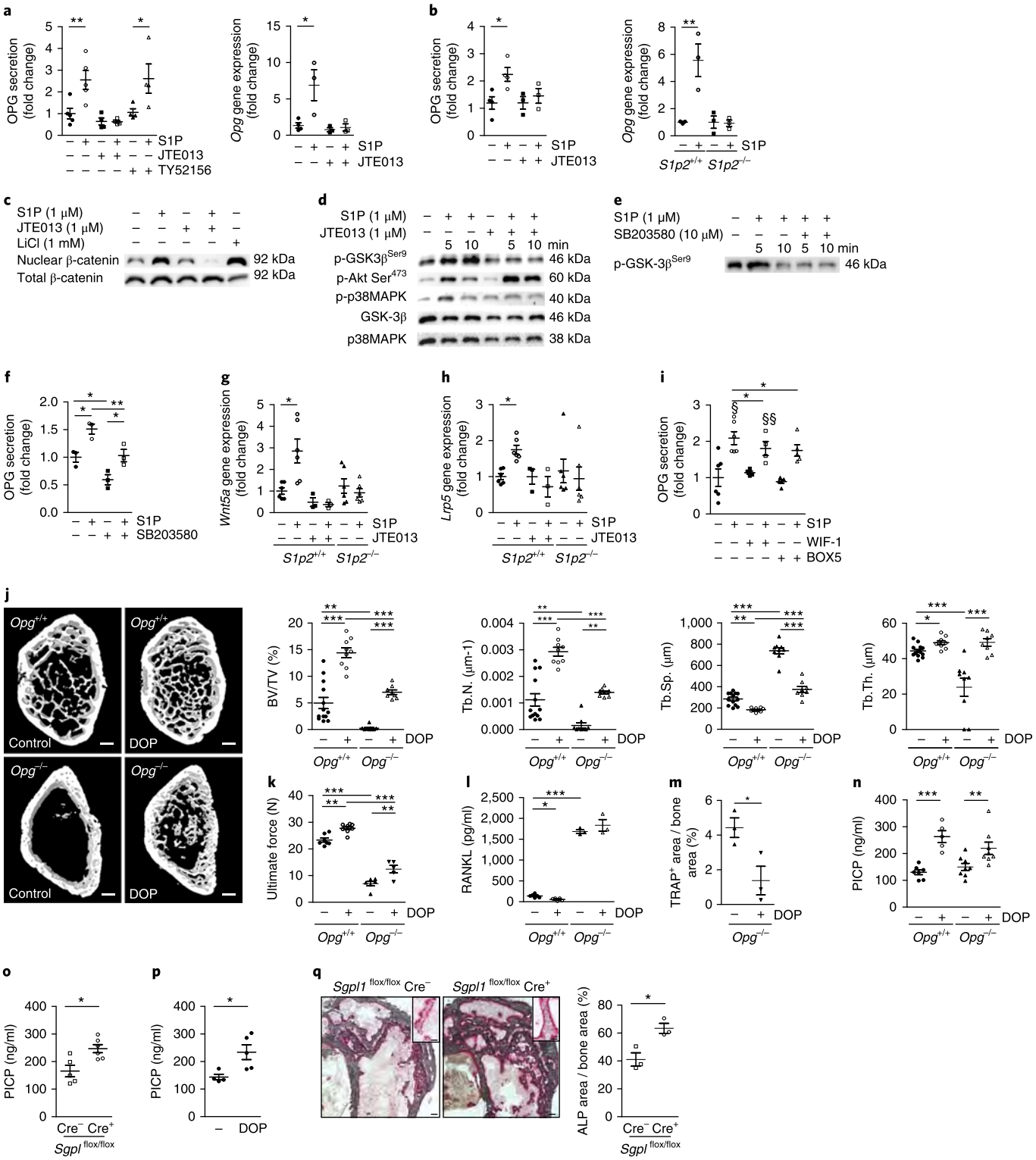

interestingly, even accelerated adipogenic differentiation in the absence of S1P (Fig. 3k).

S1P lyase deficiency or inhibition reduces white adipose tissue. To address potential relevance for these findings in vivo, we investigated whether the higher bone mass observed with elevated S1P concentrations after lyase deletion or inhibition went along with an altered adipose tissue phenotype. This was, indeed, the case: body weight and perigonadal white adipose tissue (WAT) weight of *Sgpl* KO mice were reduced by 13% and an impressive 77%, respectively, as compared to control littermates of identical sex and age (Fig. 3l). Relative WAT weight (perigonadal WAT weight per body weight) was reduced by 71% (Fig. 3l). To assess the effect of lyase deletion or inhibition not only on perigonadal depots but also other WAT depots, we performed whole-body magnetic resonance imaging (MRI) to analyze adipose tissue distribution. MRI revealed an impressive twofold-lower subcutaneous and abdominal WAT depot volumes in *Sgpl* KO mice (Fig. 3m). Histomorphometric analysis of adipocyte size demonstrated a lower mean cell size with a prominent shift toward smaller cells

(Fig. 3n and Supplementary Fig. 5a). We also observed a sixfold lower plasma leptin concentration in *Sgpl* KO mice than in controls (Supplementary Fig. 5b). Neither food intake nor feces lipid content differed between these groups of mice (Supplementary Fig. 6). Results very similar to those in *Sgpl* KO mice were obtained in DOP-treated C57BL/6J mice, in which a 20% reduction in body weight and 75% reduction in perigonadal WAT weight were observed (Supplementary Fig. 7).

***S1p2*$^{-/-}$ mice exhibit osteopenia, low plasma OPG and obesity.** A notable question was whether $S1P_2$ signaling reciprocally regulated bone and adipose tissue homeostasis in vivo. This was, indeed, the case: *S1p2*$^{-/-}$ mice were osteopenic, as demonstrated by 45% lower BV/TV, 30% lower Tb.N. and 15% lower Tb.Th. than wild-type mice of identical age and sex (Fig. 4a). The plasma OPG concentration measured in *S1p2*$^{-/-}$ mice was 39% lower than that in wild-type mice (Fig. 4b), which is in agreement with $S1P_2$ regulating OPG expression in vivo. Cortical thickness in the femoral midshaft of *S1p2*$^{-/-}$ mice was also lower than that in wild-type mice (Fig. 4c), resulting in a reduction of mechanical strength (ultimate force; Fig. 4d). Stiffness, elastic modulus and ultimate stress were not different between groups (Supplementary Fig. 8a).

The osteopenia in *S1p2*$^{-/-}$ mice was accompanied by a striking adipose tissue phenotype: body weight was 14% higher, perigonadal WAT was 70% higher, and relative WAT weight was 44% higher in *S1p2*$^{-/-}$ mice than in wild-type controls of identical sex and age (Fig. 4e). Quantitative histomorphometry also demonstrated a larger adipocyte size with a shift toward bigger cells in *S1p2*$^{-/-}$ mice (Fig. 4f and Supplementary Fig. 8b). Furthermore, bone marrow adipocytes were prevalent in *S1p2*$^{-/-}$ mice but absent in wild-type mice (Supplementary Fig. 9), indicating that mesenchymal stem cells (MSCs) differentiated toward the adipogenic lineage rather than the osteoblastogenic lineage[26].

S1P lyase inhibition raises bone mass as efficiently as iPTH, and is superior to iPTH in enhancing bone strength in ovariectomy-induced osteopenia. We next evaluated the therapeutic potential of S1P lyase inhibition in osteoporosis induced by estrogen deficiency, the most prevalent cause of osteoporosis worldwide, using the ovariectomy (OVX)-induced osteopenia model[27]. To explore therapeutic rather than prophylactic potential, OVX was performed in adult C57BL/6J mice after complete skeletal remodeling, and DOP therapy initiated after manifestation of disease (4 weeks after OVX). Furthermore, we benchmarked DOP to intermittent parathyroid hormone (iPTH) therapy, the only osteoanabolic treatment for humans. After 6 weeks of treatment, DOP showed a clear therapeutic effect: trabecular BV/TV was threefold higher, Tb.N. was 3.2-fold higher and Tb.Sp. was 32% lower in DOP-treated mice than in vehicle-treated OVX mice (Fig. 5a). This effect was comparable to that of iPTH (Fig. 5a). Cortical thickness and BMD were not altered by any treatment (Fig. 5b) but mechanical bone strength was (Fig. 5c): ultimate force, stiffness and elastic modulus were higher with both DOP and iPTH compared to controls (Fig. 5c). Remarkably, DOP was superior to iPTH in respect to raising stiffness and elastic modulus (Fig. 5c). DOP therapy was osteoanabolic: it raised PICP concentrations in plasma compared both to vehicle-treated OVX mice and iPTH-treated OVX mice (Fig. 5d). Similarly to what occurred in DOP-treated C57BL/6J mice and *Opg*$^{-/-}$ mice, it also led to a decrease in OS/BS (Fig. 5e). In addition, DOP also exhibited a clear anticatabolic effect, as PYD concentrations in plasma were lower than those in vehicle-treated OVX mice (Fig. 5f), and OC-occupied area was diminished in situ (Fig. 5g). As expected from our previous data, plasma OPG concentrations were also higher (Fig. 5h). In contrast, PICP, PYD and OPG were not altered with iPTH (Fig. 5d,g,h).

Besides osteoporosis, postmenopausal women often suffer from core obesity developing due to estrogen deficiency[28], a situation that is mirrored in the OVX model and is reversible through estrogen replacement[29]. Of note, besides its beneficial effect on osteopenia, DOP therapy effectively reduced body weight and WAT mass in OVX mice (Fig. 5i–k).

Associations of S1P with bone-related parameters in the SHIP-Trend study. To gain insights into human disease, we analyzed data obtained from 4,091 participants of a large German population-based study, the Study of Health in Pomerania (SHIP-Trend)[30] (participant characteristics are presented in Supplementary

Fig. 3 | S1P activates OB and inhibits adipocyte differentiation through $S1P_2$, and there is reduced adipose tissue mass and adipocyte size in *Sgpl*$^{flox/flox}$ Cre^{+} mice. a, Expression of genes related to OB differentiation in *S1p2*$^{+/+}$ and *S1p2*$^{-/-}$ OBs after 24 h of treatment with S1P (1 μM) or no treatment ($n = 3$ per group; fold to baseline). **b**, Calcium deposition of *S1p2*$^{+/+}$ and *S1p2*$^{-/-}$ OBs cultured in differentiation medium with or without S1P (1 μM) for 14 d ($n = 10$ untreated *S1p2*$^{+/+}$ and *S1p2*$^{-/-}$ control OBs and 6 S1P-treated *S1p2*$^{+/+}$ and *S1p2*$^{-/-}$ OBs). **c**, Proliferation of OBs from *S1p2*$^{+/+}$ and *S1p2*$^{-/-}$ mice that were untreated or treated with S1P (1 μM) daily for 6 d ($n = 3$ mice per group). **d**, *Osterix* gene expression in OBs from *S1p2*$^{+/+}$ and *S1p2*$^{-/-}$ mice that received 24 h of in vitro treatment with S1P (1 μM) or no treatment ($n = 6$ S1P-treated and untreated *S1p2*$^{+/+}$ OBs, 3 S1P-treated and untreated *S1p2*$^{-/-}$ OBs; fold to baseline). **e**, *Pparg* gene expression in OBs from *S1p2*$^{+/+}$ and *S1p2*$^{-/-}$ mice that received 24 h of in vitro treatment with S1P (1 μM) or no treatment ($n = 10$ treated and untreated *S1p2*$^{+/+}$ OBs, 3 treated and untreated *S1p2*$^{-/-}$ OBs; fold to baseline). **f**, *C/ebp-alpha* gene expression in OBs from *S1p2*$^{+/+}$ and *S1p2*$^{-/-}$ mice that received 24 h of in vitro treatment with S1P (1 μM) or no treatment ($n = 4$ treated and untreated *S1p2*$^{+/+}$ OBs, 3 treated and untreated *S1p2*$^{-/-}$ OBs; fold to baseline). **g**, Expression of genes related to adipogenic differentiation in OBs from *S1p2*$^{+/+}$ and *S1p2*$^{-/-}$ mice that received 24 h of in vitro treatment with S1P (1 μM) or no treatment ($n =$ at least 5 OBs per group and gene; fold to baseline). **h**, Expression of genes related to OB differentiation in OBs from C57BL/6J mice that received 24 h of in vitro treatment with S1P (1 μM) and/or rosiglitazone (5 μM) or no treatment (for each gene, $n = 6$ untreated and S1P-treated OBs, 3 rosiglitazone-treated OBs and S1P–rosiglitazone-treated OBs; fold to baseline). **i**, Expression of adipogenic differentiation genes in OBs from wild-type mice that received 24 h of in vitro treatment with S1P (1 μM) and/or rosiglitazone (5 μM) or no treatment (for each gene, $n = 3$ OBs per group; fold to baseline). **j**, Expression of genes related to adipogenic differentiation in 3T3-L1 cells that received 48 h of in vitro treatment with S1P (1 μM) or no treatment (for each gene, $n = 4$ OBs per group). **k**, Left, Oil Red O staining of 3T3-L1 adipocytes after 6 d of differentiation with S1P and/or JTE013 (1 μM each) or with no treatment. Right, quantification of Oil Red O staining using Cy5 fluorescence intensity (655 - 685 nm, $n = 4$ mice per group). **l**, Top, representative images of perigonadal WAT from *Sgpl*$^{flox/flox}$ Cre^{-} and *Sgpl*$^{flox/flox}$ Cre^{+} mice of the same age and sex. Bottom, quantification of body weight, WAT weight and relative WAT weight (right) of these mice ($n = 9$ mice per group). Scale bars, 5 mm. **m,** Left, representative T2-weighted axial magnetic resonance images at the level of kidneys from *Sgpl*$^{flox/flox}$ Cre^{-} and *Sgpl*$^{flox/flox}$ Cre^{+} mice. Right, quantification of fat volume showing substantially smaller fat depots in all segments (subcutaneous, visceral and renal fat) in these mice ($n = 7$ *Sgpl*$^{flox/flox}$ Cre^{-} and 5 *Sgpl*$^{flox/flox}$ Cre^{+} mice). Scale bars, 1 cm. **n**, Left, representative H&E staining of perigonadal WAT from *Sgpl*$^{flox/flox}$ Cre^{-} and *Sgpl*$^{flox/flox}$ Cre^{+} mice. Right, quantification of adipocyte size distribution in perigonadal WAT of these mice ($n = 5$ mice per group). Scale bars, 100 μm. Data are presented as mean ± s.e.m. A one-way ANOVA with Tukey's multiple-comparisons test (a–k) and a two-tailed *t*-test (l–n) were used for statistical analysis. $^{*}P < 0.05$; $^{**}P < 0.01$.

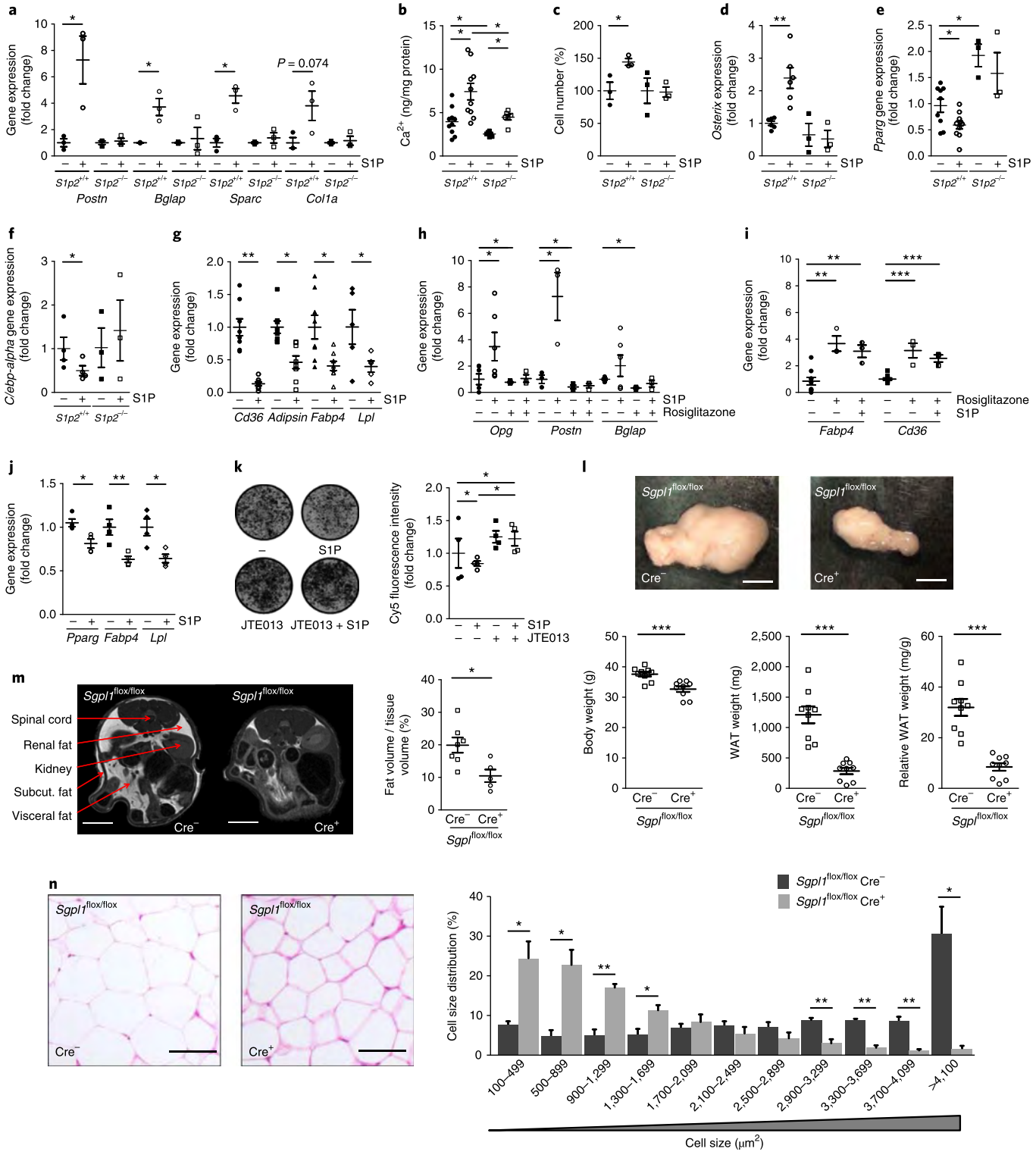

Table 1) for associations between bone-related parameters and serum S1P levels (Supplementary Table 2). We observed a strong positive association between serum S1P concentrations and the concentrations of the clinical bone formation marker procollagen type 1-N-terminal propeptide (PINP; Fig. 6a); exemplifying this, a 10 ng/ml increase in PINP concentration was related to a 2.9 pmol/ml increase in S1P concentration. In comparison, there was no association between the S1P level and that of the clinical bone resorption marker C-terminal telopeptide of type I collagen (CTX; Fig. 6b). Serum S1P concentrations also correlated positively with concentrations of calcium and inversely with PTH levels (Fig. 6c,d).

The golden standard in the diagnosis of osteoporosis is the assessment of bone mineral density using dual X-ray absorptiometry (DXA). This was not feasible in a population-based study, such as SHIP-Trend, for ethical reasons. Therefore, we substituted DXA with quantitative ultrasound (QUS) measurements at the heel, a method with similarly reliable fracture risk prediction[31]. Using the QUS-based bone stiffness index, we observed an inverse relation between bone mineral density and S1P concentration (Fig. 6e).

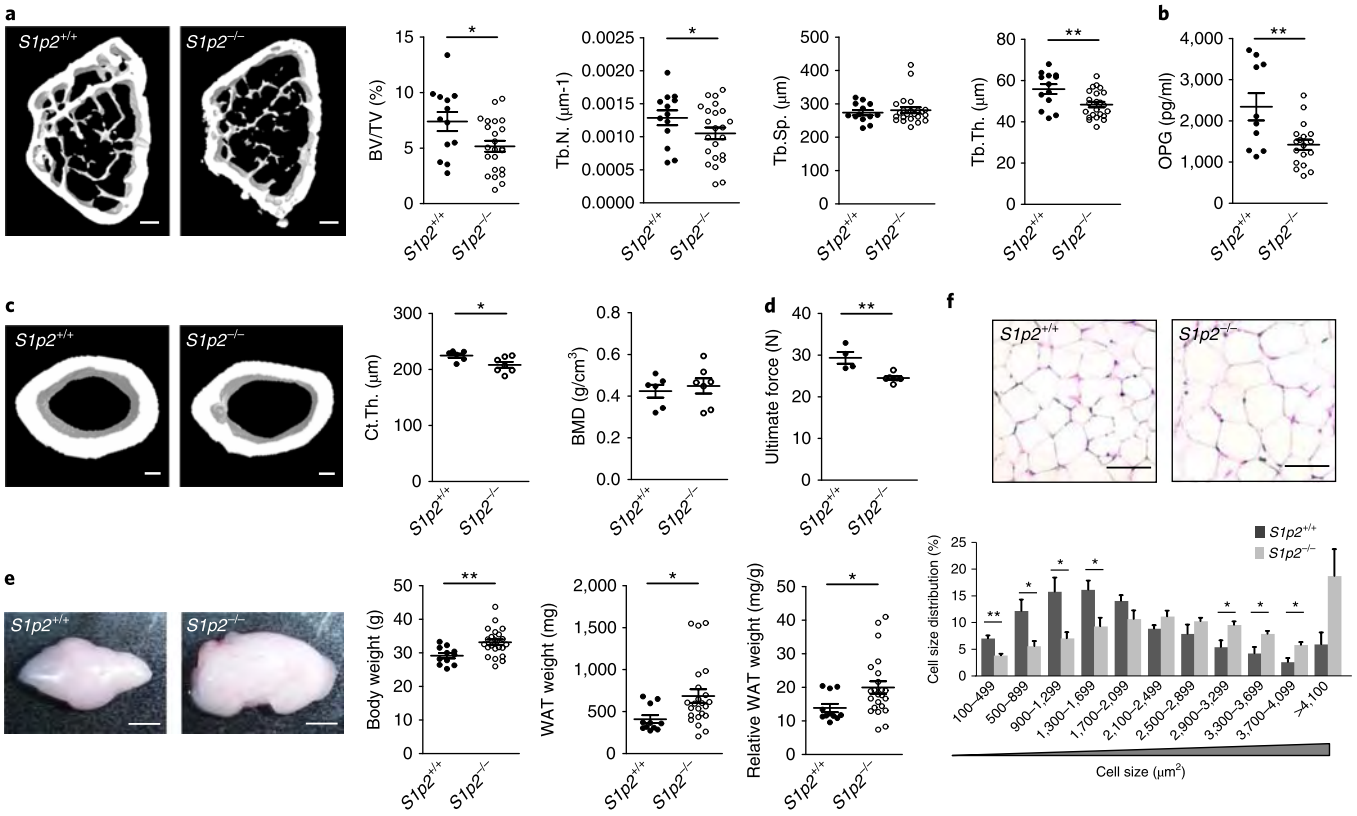

Fig. 4 | S1P2 deficiency results in the development of osteopenia and obesity. a, Left, μCT analysis of the spongiosa in the femoral metaphysis of male *S1p2*$^{+/+}$ and *S1p2*$^{-/-}$ mice aged 25 weeks ($n=13$ *S1p2*$^{+/+}$ mice, 23 *S1p2*$^{-/-}$ mice). Representative images (left) and quantification of trabecular BV/TV, Tb.N., Tb.Sp. and Tb.Th. (right) are shown. Scale bars, 350 μm. **b**, OPG concentration in plasma from *S1p2*$^{+/+}$ and *S1p2*$^{-/-}$ mice aged 25 weeks ($n=10$ *S1p2*$^{+/+}$ mice, 18 *S1p2*$^{-/-}$ mice). **c**, Left, μCT analysis of the corticalis at the femoral midshaft of male *S1p2*$^{+/+}$ and *S1p2*$^{-/-}$ mice aged 25 weeks ($n=14$ *S1p2*$^{+/+}$ mice, 13 *S1p2*$^{-/-}$ mice). Scale bars, 200 μm. **d**, Ultimate force in the three-point bending test of the femoral midshafts of *S1p2*$^{+/+}$ and *S1p2*$^{-/-}$ mice aged 25 weeks ($n=4$ *S1p2*$^{+/+}$ mice, 6 *S1p2*$^{-/-}$ mice) . **e**, Left, representative images of perigonadal WAT of male *S1p2*$^{+/+}$ and *S1p2*$^{-/-}$ mice aged 25 weeks. Right, body weight, WAT weight and relative WAT weight of *S1p2*$^{+/+}$ and *S1p2*$^{-/-}$ mice aged 25 weeks ($n=11$ *S1p2*$^{+/+}$ mice, 23 *S1p2*$^{-/-}$ mice). **f**, Top, representative H&E staining of perigonadal WAT of *S1p2*$^{+/+}$ and *S1p2*$^{-/-}$ mice aged 25 weeks. Bottom, quantification of adipocyte size distribution in perigonadal WAT of these mice ($n=6$ mice per group). Scale bars, 100 μm. Data are presented as mean ± s.e.m. A two-tailed *t*-test was used for statistical analysis. $^{*}P<0.05$; $^{**}P<0.01$.

The QUS-based bone stiffness index was also inversely related to the serum concentration of the bone-formation marker PINP (Fig. 6f). This indicated that bone anabolic activity and S1P both increase with decreasing bone quality.

There was also an intriguing curvilinear association between S1P and body mass index (BMI) after adjustment for sex and age: S1P concentrations increased with BMI up to a threshold of about 30 kg/m^2, the cut-off for obesity, and decreased thereafter with a further increase in BMI (Fig. 6g and Supplementary Table 2).

Discussion

There are currently 200 million people suffering from osteoporosis worldwide[32]. Low bone mass and deteriorating bone quality lead to an increased risk of fractures, high morbidity and, in men, increased mortality[33]. According to the International Osteoporosis Foundation, one in three women and one in five men over the age of 50 will experience osteoporotic fractures in their lifetime. Current pharmacological therapy consists of antiresorptive agents[33], none of which stimulates new bone formation, and rPTH (teriparatide) as the only osteoanabolic treatment approved so far. It is restricted to women with postmenopausal osteoporosis who are at high risk for fracture and are resistant or intolerant to other therapy and to men with idiopathic or hypogonadal osteoporosis. However, it has a 'black box' warning because of the occurrence of osteosarcomas in rats following treatment; also, it must be paused after 2 years, limiting its usefulness for life-long treatment. Currently, antisclerostin therapy is being assessed as a new approach in phase 3 clinical studies, but there are concerns about cardiovascular side effects[34].

We show here that S1P-based agents have the potential to become new osteoanabolic drugs with additional antiresorptive properties. Compared with the strictly osteoanabolic rPTH in the OVX model, pharmacological S1P lyase inhibition was equipotent in increasing new bone formation and superior in promoting bone strength. In our study, we have identified several nonredundant mechanisms underlying such a unique dual impact of S1P on bone homeostasis (Fig. 6h). The antiresorptive capacity of S1P originated from the stimulation of OPG production through two different pathways that were both mediated by the OB $S1P_2$ receptor (Fig. 6i). The first involved activation of a newly discovered p38-dependent GSK3β–β-catenin pathway, whereas the second relied on transcriptional stimulation of WNT5A. Both pathways acted together to ensure an overlapping, persistent stimulation of OPG production (Fig. 6i). The evidence for causal $S1P_2$ involvement in OPG production is unambiguous: (i) *S1p2*$^{-/-}$ mice displayed reduced plasma OPG levels; (ii) $S1P_2$ inhibition and deficiency in OBs prevented OPG production and (iii) FTY720, a S1P prodrug that after its phosphorylation acts on all S1P receptors but $S1P_2$, had no effect.

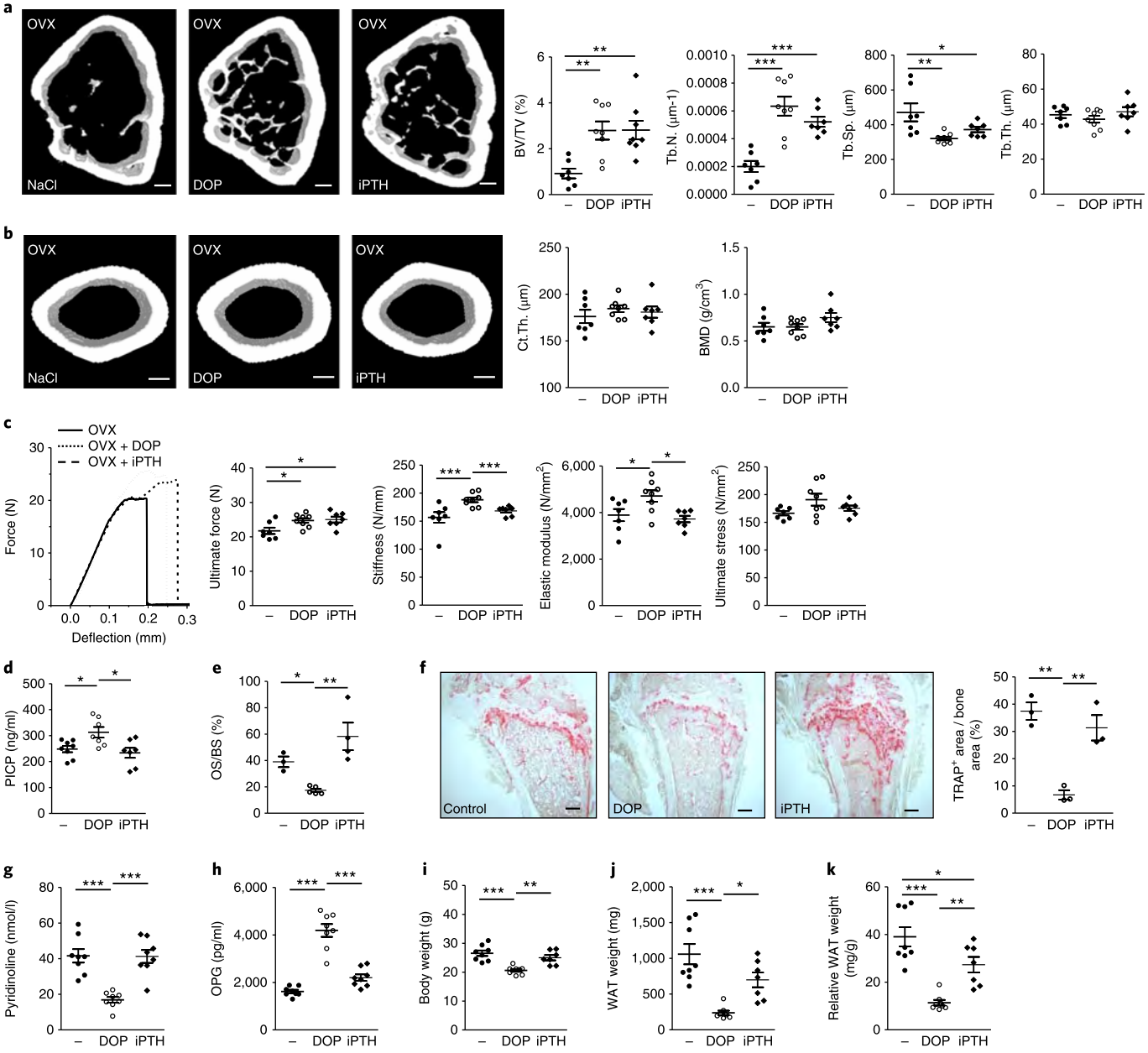

Fig. 5 | DOP treatment of OVX mice increases trabecular bone volume and mechanical strength, elevates levels of bone formation markers and OPG in plasma and reduces levels of bone resorption markers. a,**b**, Left, μCT analysis of trabecular bone in the femoral metaphysis (**a**) and of the femoral corticalis at midshaft (**b**) in female OVX mice aged 22 weeks that were treated with vehicle (NaCl), iPTH and DOP for 6 weeks. Right, quantification of various parameters in these mice ($n = 7$ NaCl- and iPTH-treated mice, 8 DOP-treated mice). Scale bars, 350 μm (**a**), 200 μm (**b**). **c**, Ultimate force, stiffness, elastic modulus and ultimate stress in the three-point bending test of the femoral midshafts of the same mice as in **a** and **b**. Representative curves (left) and quantification (right) are shown. **d**,**e**, Concentration of PICP in plasma (**d**; $n = 7$ vehicle- and iPTH-treated OVX mice, 8 DOP-treated OVX mice) and OS/BS (e; $n = 3$ vehicle-treated OVX mice, 5 DOP-treated OVX mice, 4 iPTH-treated OVX mice) of the same mice as in a and b. **f**, Representative images (left) and histomorphometric analysis (right) of TRAP staining of tibiae of the same vehicle, iPTH and DOP treated OVX mice ($n = 3$ mice per group). Scale bars, 200 μm. **g**,**h**, Concentration of pyridinoline cross-links (**g**) and OPG (**h**) in plasma of the same mice ($n = 7$ vehicle- and iPTH-treated OVX mice, 8 DOP-treated OVX mice). **i**–**k**, Body weight (**i**) and weight of WAT (**j**) and relative WAT (**k**) in the same mice ($n = 7$ vehicle- and iPTH-treated OVX mice, 8 DOP-treated OVX mice). Data are presented as mean ± s.e.m. A one-way ANOVA with Tukey's multiple-comparisons test was used for statistical analysis. $^*P < 0.05$; $^{**}P < 0.01$; $^{***}P < 0.001$.

The second, osteoanabolic component of S1P and $S1P_2$ signaling was derived from the potent induction of OB differentiation, proliferation and mineralization in vitro and in vivo (Fig. 6h). A higher Tb.N. rather than increased thickness through stimulation of S1P signaling, a higher MAR accompanied by a lower OS/BS, a larger trabecular ALP surface area and a higher plasma concentration of the clinically validated bone-formation marker PICP in vivo along with the induction of OB differentiation and mineralization in vitro led us to conclude that S1P, indeed, promotes genuine formation of new bone. The effect of S1P was a true promotion of bone accrual and not merely a prevention of bone loss, evidenced by the fact that all these parameters did not change in

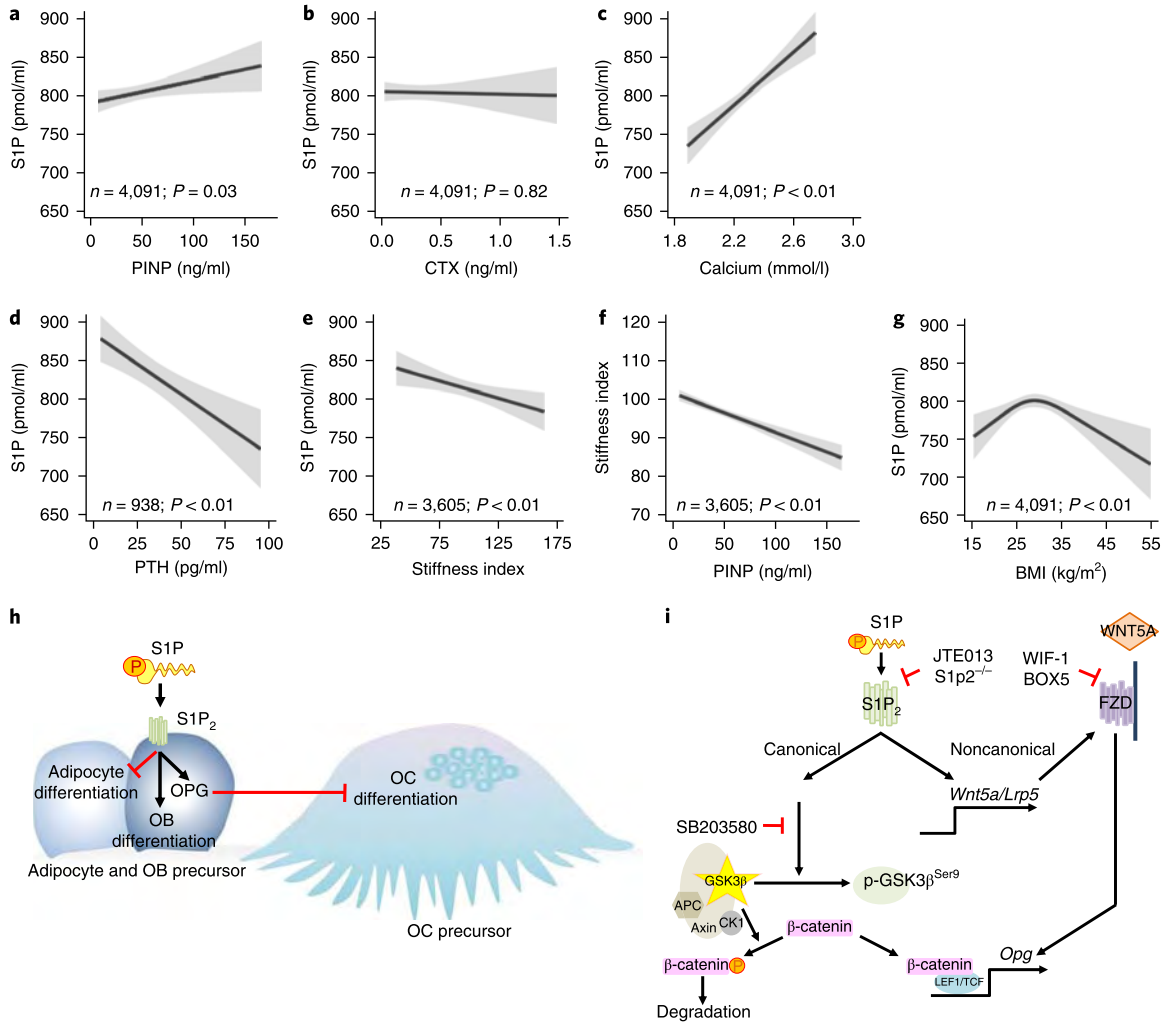

Fig. 6 | Association of serum S1P levels and with various bone-related parameters in humans. a–e, Association between serum S1P and bone formation (**a**) and resorption markers (**b**), calcium levels (**c**), PTH levels (**d**), and stiffness index (**e**) in 4,091 human subjects in the SHIP-Trend study population. **f**, Association between stiffness index and serum PINP. **g**, Association between serum S1P and BMI. All results in **a–g** are from multivariable linear regression analyses. All models but BMI were adjusted for age, sex and BMI. The association between BMI and S1P was adjusted for age and sex and was nonlinear; therefore, restricted cubic splines with three knots were applied. The solid black line represents the estimated S1P concentrations for an average man (aged 53 years; BMI, 27 kg/m^2) from the study population; the shaded gray area represents the 95% confidence interval. **h**, Schematic of the overall role of S1P in bone homeostasis based on our findings. **i**, Schematic of the two different mechanisms involved in OPG induction by S1P (APC = adenomatous polyposis coli; FZD = frizzled; CK1= casein kinase 1).

untreated mice over the same period of time as that when the experimental cohort received DOP (Supplementary Fig. 10). Only BMD declined and elastic modulus increased, and both of these effects were prevented by DOP (Supplementary Fig. 10). The increase in bone mass was strikingly prominent even in the complete absence of OPG, suggesting that the OB-related effect of S1P was, indeed, extremely efficient. MSCs are capable of developing into OBs, adipocytes, chondrocytes or fibroblasts[22]; the commitment to the OB or adipocyte lineage depends on the orchestrated action of adipogenic and osteoblastogenic transcription factors[35–37]. These factors also influence each other and regulate cell fate together over many steps of the differentiation process: overexpression of *Runx2* or *Osterix* in adipose tissue–derived MSCs and even in 3T3-L1 adipogenic precursors results in the generation of functional OBs[38–40], whereas *Pparg2* overexpression in osteoblastic MC3T3-E1 cells induces transdifferentiation into adipocytes[41]. Furthermore, PPAR-γ and C/EBP-α promote adipogenesis not only directly but also via suppressing osteogenesis through inhibition of RUNX2 and β-catenin[42–44]. Wnt signaling also has an important role in the commitment process[26,45] because loss of Wnt–β-catenin signaling in preosteoblasts transforms them into adipocytes[26], whereas WNT5A activation potently inhibits PPAR-γ and adipogenesis[46,47]. In contrast, rosiglitazone causes bone loss not only by downregulating expression of *Runx2*, *Osterix* and *Opg* but also the WNT5A-receptor-encoding gene *Fzd4*[48,49]. We found that S1P induced expression of *Osterix* and *Wnt5a* and suppressed that of *Pparg* and *Cebpa* in OB and adipocyte progenitors and, accordingly, accelerated osteoblastogenesis and suppressed adipogenesis. Most importantly, this was prevented by rosiglitazone, suggesting that S1P is a negative regulator of PPAR-γ. In support, a recent report has shown that S1P enhanced OB differentiation of human MSCs while simultaneously inhibiting their adipogenic potential[50]. We have not been able to prevent PPAR-γ suppression by S1P through Wnt inhibitors (data not shown), but Wnts are not the only link between S1P and PPAR-γ, as there is evidence of nuclear G protein–coupled receptors and substituent fragments modulating gene transcription[51]. There

are even reports on direct physical interactions between PPAR-γ and S1P or modified forms of lysophosphatidic acid[52].

Cell fate decisions also take place in stromal cells derived from visceral adipose tissue that apparently possess an osteogenic potential similar to that of bone marrow MSCs[53]. Remarkably, adipose tissue–derived stem cells have been found to be responsible for 10% of the annual adipocyte turnover at all adult ages and levels of BMI[54]. Thus, S1P may be promoting not only ostoblastogenic differentiation at the expense of adipocytic differentiation in bone marrow–derived MSCs but also inhibiting the differentiation of genuine adipose tissue stem cells. Indeed, mice with deletion or inhibition of S1P lyase developed a striking lean phenotype evidenced by the substantial reduction in all WAT depots, whereas *S1p2*$^{-/-}$ mice were osteopenic and obese. This suggests that tonic (continuous) $S1P_2$ signaling is required to keep adipose tissue differentiation at bay and that additional stimulation further suppresses it. S1P has been shown to have anti-adipogenic effects in preadipocyte cultures in vitro, and plasma S1P concentrations have been suspected to have a connection to adipose tissue mass, but the picture is rather obscure considering that not only obesity but also physical exercise and fasting result in higher plasma S1P concentrations[55]. Our findings on BMI and S1P in over 4,000 human participants of the SHIP-Trend study may help resolve such discrepancies; we have observed an intriguing curvilinear association between S1P and BMI, with S1P increasing up to a BMI of 30 kg/m^2, the cut-off for obesity, and declining thereafter with increasing obesity.

In humans, we have performed the largest investigation to date of S1P associations with bone-related parameters using data from 4,091 participants of the large population-based SHIP-Trend study . Very little data are available on the relationship between human bone health or disease and S1P; a recent study in postmenopausal Korean women[56] has found a negative association between S1P and BMD at some sites (trochanter and femoral shaft) but not at others (femoral neck or lumbar spine) and a marginally positive association with bone resorption markers (CTX), whereas none was found with bone formation markers. In a 3.5-year follow up of the same population (some members had therapy, and others did not), a higher incident fracture risk (albeit at extremely low numbers) was found to be associated with a higher S1P level at admission[57]. However, fracture risk did not differ between groups, and S1P concentrations were not monitored[57]. This purely observational association of S1P with bone quality is similar to ours, but we draw the exactly opposite conclusion: high S1P is not detrimental for bone mass but, instead, serves as a counter-regulatory measure to increase bone mass in response to decreasing bone quality. Indeed, the highly significant positive association between plasma levels of the clinical bone formation marker PINP with S1P and the negative association of both of these with the QUS-based stiffness index suggest that S1P is a driver of bone formation. These associations were largely unaffected by age, as the change in β-coefficients was no more than 10% without age adjustment, and the *P* values remained unchanged (data not shown). Indeed, every experimental approach that we undertook to increase S1P concentration and $S1P_2$ signaling both in normal and osteoporotic or osteopenic mice inevitably led to higher bone formation, lower bone resorption and an appreciable increase of bone mass and strength. The lack of negative association between S1P and CTX in contrast to the clearly positive association between S1P and PINP in our population-based cohort may suggest a higher sensitivity of bone formation than bone resorption to S1P. The positive association of S1P with calcium and the inverse association of S1P with PTH further support this notion and require further study. As systemic inhibition of S1P lyase is known to cause lymphopenia, bone-homing methods[58,59] for drug delivery to knockdown the enzyme specifically in OBs could offer more bone specificity to this approach.

In the past few years, obesity and osteoporosis have been increasingly linked mechanistically[60]. Thus, a therapeutic approach that beneficially affects both diseases by impacting common regulatory mechanisms would be highly useful. Indeed, targeting S1P metabolism and receptors may favorably affect both osteoporosis and core obesity developing in postmenopausal women in response to estrogen deficiency[28]. Furthermore, the striking increase in bone mass in *Opg*$^{-/-}$ mice bears promising clinical potential for new therapies of debilitating genetic bone diseases, such as juvenile Paget disease 1, the severe osteoporosis caused by genetic defects in *Opg*. Any treatment success in rare bone diseases would lay the foundations for much broader indications and initiate large clinical studies in the general population.

Methods

Methods, including statements of data availability and any associated accession codes and references, are available at https://doi.org/10.1038/s41591-018-0005-y.

Received: 11 January 2017; Accepted: 13 February 2018;
Published online: 16 April 2018

References

1. Maceyka, M., Harikumar, K. B., Milstien, S. & Spiegel, S. Sphingosine-1-phosphate signaling and its role in disease. *Trends Cell Biol.* **22**, 50–60 (2012).
2. Takabe, K., Paugh, S. W., Milstien, S. & Spiegel, S. "Inside-out" signaling of sphingosine-1-phosphate: therapeutic targets. *Pharmacol. Rev.* **60**, 181–195 (2008).
3. Rosen, H., Stevens, R. C., Hanson, M., Roberts, E. & Oldstone, M. B. Sphingosine-1-phosphate and its receptors: structure, signaling, and influence. *Annu. Rev. Biochem.* **82**, 637–662 (2013).
4. Kunkel, G. T., Maceyka, M., Milstien, S. & Spiegel, S. Targeting the sphingosine-1-phosphate axis in cancer, inflammation and beyond. *Nat. Rev. Drug Discov.* **12**, 688–702 (2013).
5. Teitelbaum, S. L. Bone resorption by osteoclasts. *Science* **289**, 1504–1508 (2000).
6. Ishii, M. & Kikuta, J. Sphingosine-1-phosphate signaling controlling osteoclasts and bone homeostasis. *Biochim. Biophys. Acta* **1831**, 223–227 (2013).
7. Keller, J. et al. Calcitonin controls bone formation by inhibiting the release of sphingosine 1-phosphate from osteoclasts. *Nat. Commun.* **5**, 5215 (2014).
8. Ryu, J. et al. Sphingosine 1-phosphate as a regulator of osteoclast differentiation and osteoclast-osteoblast coupling. *EMBO J.* **25**, 5840–5851 (2006).
9. Ishii, M., Kikuta, J., Shimazu, Y., Meier-Schellersheim, M. & Germain, R. N. Chemorepulsion by blood S1P regulates osteoclast precursor mobilization and bone remodeling in vivo. *J. Exp. Med.* **207**, 2793–2798 (2010).
10. Ishii, T., Shimazu, Y., Nishiyama, I., Kikuta, J. & Ishii, M. The role of sphingosine 1-phosphate in migration of osteoclast precursors; an application of intravital two-photon microscopy. *Mol. Cells* **31**, 399–403 (2011).
11. Pederson, L., Ruan, M., Westendorf, J. J., Khosla, S. & Oursler, M. J. Regulation of bone formation by osteoclasts involves Wnt/BMP signaling and the chemokine sphingosine-1-phosphate. *Proc. Natl. Acad. Sci. USA* **105**, 20764–20769 (2008).
12. Lotinun, S. et al. Osteoclast-specific cathepsin K deletion stimulates S1P-dependent bone formation. *J. Clin. Invest.* **123**, 666–681 (2013).
13. Vogel, P. et al. Incomplete inhibition of sphingosine 1-phosphate lyase modulates immune system function yet prevents early lethality and non-lymphoid lesions. *PLoS One* **4**, e4112 (2009).
14. Billich, A. et al. Partial deficiency of sphingosine-1-phosphate lyase confers protection in experimental autoimmune encephalomyelitis. *PLoS One* **8**, e59630 (2013).
15. Pelletier, D. & Hafler, D. A. Fingolimod for multiple sclerosis. *N. Engl. J. Med.* **366**, 339–347 (2012).
16. Khosla, S. Minireview: the OPG/RANKL/RANK system. *Endocrinology* **142**, 5050–5055 (2001).
17. Boyce, B. F., Xing, L. & Chen, D. Osteoprotegerin, the bone protector, is a surprising target for beta-catenin signaling. *Cell Metab.* **2**, 344–345 (2005).
18. Yokoyama, N., Yin, D. & Malbon, C. C. Abundance, complexation, and trafficking of Wnt/beta-catenin signaling elements in response to Wnt3a. *J. Mol. Signal* **2**, 11 (2007).

19. Bikkavilli, R. K., Feigin, M. E. & Malbon, C. C. p38 mitogen-activated protein kinase regulates canonical Wnt-β-catenin signaling by inactivation of GSK3β. *J. Cell Sci.* **121**, 3598–3607 (2008).
20. Spencer, G. J., Utting, J. C., Etheridge, S. L., Arnett, T. R. & Genever, P. G. Wnt signalling in osteoblasts regulates expression of the receptor activator of NFκ ligand and inhibits osteoclastogenesis in vitro. *J. Cell Sci.* **119**, 1283–1296 (2006).
21. Mizuno, A. et al. Severe osteoporosis in mice lacking osteoclastogenesis inhibitory factor/osteoprotegerin. *Biochem. Biophys. Res. Commun.* **247**, 610–615 (1998).
22. Pittenger, M. F. et al. Multilineage potential of adult human mesenchymal stem cells. *Science* **284**, 143–147 (1999).
23. Linhart, H. G. et al. C/EBPα is required for differentiation of white, but not brown, adipose tissue. *Proc. Natl. Acad. Sci. USA* **98**, 12532–12537 (2001).
24. Kang, S. et al. Wnt signaling stimulates osteoblastogenesis of mesenchymal precursors by suppressing CCAAT/enhancer-binding protein α and peroxisome proliferator-activated receptor γ. *J. Biol. Chem.* **282**, 14515–14524 (2007).
25. Yu, W. H. et al. PPARγ suppression inhibits adipogenesis but does not promote osteogenesis of human mesenchymal stem cells. *Int. J. Biochem. Cell Biol.* **44**, 377–384 (2012).
26. Song, L. et al. Loss of wnt/beta-catenin signaling causes cell fate shift of preosteoblasts from osteoblasts to adipocytes. *J. Bone Miner. Res.* **27**, 2344–2358 (2012).
27. Jee, W. S. & Yao, W. Overview: animal models of osteopenia and osteoporosis. *J. Musculoskelet. Neuronal Interact.* **1**, 193–207 (2001).
28. Carr, M. C. The emergence of the metabolic syndrome with menopause. *J. Clin. Endocrinol. Metab.* **88**, 2404–2411 (2003).
29. Stubbins, R. E., Holcomb, V. B., Hong, J. & Núñez, N. P. Estrogen modulates abdominal adiposity and protects female mice from obesity and impaired glucose tolerance. *Eur. J. Nutr.* **51**, 861–870 (2012).
30. Völzke, H. et al. Cohort profile: the study of health in Pomerania. *Int. J. Epidemiol.* **40**, 294–307 (2011).
31. Hans, D. et al. Ultrasonographic heel measurements to predict hip fracture in elderly women: the EPIDOS prospective study. *Lancet* **348**, 511–514 (1996).
32. Cosman, F. et al. Clinician's guide to prevention and treatment of osteoporosis. *Osteoporos. Int.* **25**, 2359–2381 (2014).
33. Wright, N. C. et al. The recent prevalence of osteoporosis and low bone mass in the United States based on bone mineral density at the femoral neck or lumbar spine. *J. Bone Miner. Res.* **29**, 2520–2526 (2014).
34. McClung, M. R. Clinical utility of anti-sclerostin antibodies. *Bone* **96**, 3–7 (2017).
35. Ducy, P., Zhang, R., Geoffroy, V., Ridall, A. L. & Karsenty, G. Osf2/Cbfa1: a transcriptional activator of osteoblast differentiation. *Cell* **89**, 747–754 (1997).
36. Rosen, E. D. et al. C/EBPα induces adipogenesis through PPARγ: a unified pathway. *Genes Dev.* **16**, 22–26 (2002).
37. Zhang, C. Transcriptional regulation of bone formation by the osteoblast-specific transcription factor Osx. *J. Orthop. Surg. Res.* **5**, 37 (2010).
38. Halvorsen, Y. D. et al. Extracellular matrix mineralization and osteoblast gene expression by human adipose tissue-derived stromal cells. *Tissue Eng.* **7**, 729–741 (2001).
39. Takahashi, T. Overexpression of Runx2 and MKP-1 stimulates transdifferentiation of 3T3-L1 preadipocytes into bone-forming osteoblasts in vitro. *Calcif. Tissue Int.* **88**, 336–347 (2011).
40. Wu, L. et al. Osteogenic differentiation of adipose derived stem cells promoted by overexpression of osterix. *Mol. Cell. Biochem.* **301**, 83–92 (2007).
41. Kim, S. W., Her, S. J., Kim, S. Y. & Shin, C. S. Ectopic overexpression of adipogenic transcription factors induces transdifferentiation of MC3T3-E1 osteoblasts. *Biochem. Biophys. Res. Commun.* **327**, 811–819 (2005).
42. Lecka-Czernik, B. et al. Inhibition of Osf2/Cbfa1 expression and terminal osteoblast differentiation by PPARγ2. *J. Cell. Biochem.* **74**, 357–371 (1999).
43. Moldes, M. et al. Peroxisome-proliferator-activated receptor γ suppresses Wnt/β-catenin signalling during adipogenesis. *Biochem. J.* **376**, 607–613 (2003).
44. Wu, Z. et al. Cross-regulation of C/EBP α and PPAR γ controls the transcriptional pathway of adipogenesis and insulin sensitivity. *Mol. Cell* **3**, 151–158 (1999).
45. Gaur, T. et al. Canonical WNT signaling promotes osteogenesis by directly stimulating *Runx2* gene expression. *J. Biol. Chem.* **280**, 33132–33140 (2005).
46. Günther, T. & Schüle, R. Fat or bone? A non-canonical decision. *Nat. Cell Biol.* **9**, 1229–1231 (2007).
47. Zioco, E. et al. Adipocytes WNT5a mediated dedifferentiation: a possible target in pancreatic cancer microenvironment. *Oncotarget* **7**, 20223–20235 (2016).
48. Ali, A. A. et al. Rosiglitazone causes bone loss in mice by suppressing osteoblast differentiation and bone formation. *Endocrinology* **146**, 1226–1235 (2005).
49. Shockley, K. R. et al. PPARγ2 nuclear receptor controls multiple regulatory pathways of osteoblast differentiation from marrow mesenchymal stem cells. *J. Cell. Biochem.* **106**, 232–246 (2009).
50. Hashimoto, Y. et al. Sphingosine-1-phosphate inhibits differentiation of C3H10T1/2 cells into adipocyte. *Mol. Cell. Biochem.* **401**, 39–47 (2015).
51. Goetzl, E. J. Diverse pathways for nuclear signaling by G protein–coupled receptors and their ligands. *FASEB J.* **21**, 638–642 (2007).
52. Parham, K. A. et al. Sphingosine 1-phosphate is a ligand for peroxisome proliferator-activated receptor-gamma that regulates neoangiogenesis. *FASEB J.* **29**, 3638–3653 (2015).
53. Peptan, I. A., Hong, L. & Mao, J. J. Comparison of osteogenic potentials of visceral and subcutaneous adipose-derived cells of rabbits. *Plast. Reconstr. Surg.* **117**, 1462–1470 (2006).
54. Spalding, K. L. et al. Dynamics of fat cell turnover in humans. *Nature* **453**, 783–787 (2008).
55. Kowalski, G. M., Carey, A. L., Selathurai, A., Kingwell, B. A. & Bruce, C. R. Plasma sphingosine-1-phosphate is elevated in obesity. *PLoS One* **8**, e72449 (2013).
56. Lee, S. H. et al. Higher circulating sphingosine 1-phosphate levels are associated with lower bone mineral density and higher bone resorption marker in humans. *J. Clin. Endocrinol. Metab.* **97**, E1421–E1428 (2012).
57. Bae, S.J. et al. The circulating sphingosine-1-phosphate level predicts incident fracture in postmenopausal woman: a 3.5-year follow-up observation study. *Osteoporos. Int.* **27**, 2533-2541 (2016).
58. Zhang, G. et al. A delivery system targeting bone formation surfaces to facilitate RNAi-based anabolic therapy. *Nat. Med.* **18**, 307–314 (2012).
59. Liang, C. et al. Aptamer-functionalized lipid nanoparticles targeting osteoblasts as a novel RNA interference-based bone anabolic strategy. *Nat. Med* **21**, 288–294 (2015).
60. Zhao, L. J. et al. Correlation of obesity and osteoporosis: effect of fat mass on the determination of osteoporosis. *J. Bone Miner. Res.* **23**, 17–29 (2008).

Acknowledgements

We gratefully acknowledge excellent technical help by Kerstin Abou Hamed, forthcoming support by the Zentrales Tierlabor, Universitätsklinikum Essen (G. Hilken, P. Dammann, A. Wissmann, R. Waldschütz) and stimulating discussions with A. Levkau. I dedicate this work to my father, Lubomir Levkau. This work was supported in part by the Deutsche Forschungsgemeinschaft, GRK 2098, projects 9-11 (B.L., P.K.), SFB 1116, projects A08 (J.W.F.) and B02, B05 (U.F.). The work was also supported by the Alexander von Humboldt Foundation through a research fellowship awarded to M.V. The SHIP-Trend study is part of the Community Medicine Research net of the University of Greifswald, Germany, funded by the Federal Ministry of Education and Research (Grants 01ZZ9603, 01ZZ0103, and 01ZZ0403), the Ministry of Cultural Affairs and the Social Ministry of the Federal State of Mecklenburg-West Pomerania. This work was also funded in part by grants from the Deutsches Zentrum für Herz-Kreislauf-Forschung e.V. (B.H.R., M.D., E.S.).

Author contributions

S.W., M.V., A.R., K.v.W.L., J.K.B., P.K., J.N., M.E., U.F., E.S., M.D., E.M., H.V. and M.S. performed research, collected, analyzed and interpreted data, performed statistical analysis and wrote the manuscript. J.W.F., G.H., M.S. and M.H.G. contributed vital reagents or analytical tools and interpreted data. S.W., A.H., B.H.R. and B.L. designed research, analyzed and interpreted data and wrote the manuscript.

Competing interests

The authors declare no competing interests.

Additional information

Supplementary information is available for this paper at https://doi.org/10.1038/s41591-018-0005-y.

Reprints and permissions information is available at www.nature.com/reprints.

Correspondence and requests for materials should be addressed to B.L.

Publisher's note: Springer Nature remains neutral with regard to jurisdictional claims in published maps and institutional affiliations.

Methods

General experimental approaches. No samples, mice or data points were excluded from the analyses, and reported samples were not randomized to experimental groups except as specifically indicated below. Analyses were not performed in a blinded fashion except as noted below.

Human subjects and SHIP study population. Data were obtained from the baseline survey of the second cohort of SHIP-Trend, a population-based study conducted in West Pomerania, Germany. Details on study design, sampling methods and examination protocols have been reported elsewhere[30]. In short, a stratified representative sample of 10,000 (net sample size, 8,826) was drawn, and 4,420 individuals aged 20–79 years participated in baseline examinations between 2008 and 2012. All participants underwent standardized medical examinations, including blood sampling and an extensive computer-aided personal interview on health-related lifestyle and medical histories[30]. During the physical examination, height and weight were measured with calibrated scales, and BMI was calculated using the following formula: BMI = weight (kg)/height (m)2. Selection criteria that were applied to the SHIP-Trend study population are shown in Supplementary Fig. 11. Serum calcium, PINP, CTX and S1P concentrations were measured in the whole study population; serum PTH concentrations were measured in a subsample. This subsample consisted of the first 1,000 SHIP-Trend participants without diabetes mellitus. Bone quality was assessed through quantitative ultrasound (QUS) at the heel using the the Achilles InSight device (GE Medical Systems Ultrasound, GE Healthcare, Chalfont St Giles, UK). QUS measurements were offered to all SHIP-Trend participants who were examined in the main examination center ($n = 3{,}938$; 89%). The remaining participants were examined in mobile examination centers and could not opt for the QUS measurement. Moreover, we did not obtain or analyze QUS data from participants with implants, prostheses or amputations in or below the knee, open wounds or infections below the knee, injuries or surgeries during the last twelve months before the SHIP examination, incorrect positioning of the feet during the QUS measurement or wheelchair use. The present analyses were performed after exclusion of all individuals (overlap exists) for whom information regarding serum S1P ($n = 226$), PINP ($n = 119$), CTX ($n = 171$) or calcium concentrations ($n = 12$) was missing or who were outliers in these parameters; also, individuals who had missing information on BMI ($n = 7$) were excluded. This resulted in a study population of 4,091 subjects. After further exclusion of subjects without measurement of QUS ($n = 486$) or PTH ($n = 3{,}153$), subpopulations of 3,605 or 938 subjects, respectively, remained. Details on sample selection, laboratory measurements and physical examinations are given in the supplementary material (Supplementary Tables 1,2 and Supplementary Fig. 12). All participants provided written informed consent. The study conformed to the principles of the Declaration of Helsinki, as reflected by an a priori approval of the Ethics Committee of the University of Greifswald.

Mouse models. Regular and ovariectomized C57BL/6 J mice were obtained from Charles River Laboratories. *S1p2*$^{-/-}$ mice were kindly provided by J. Chun (Scripps Research Institute); inducible S1P lyase–knockout mice were provided by A. Billich (Novartis), and *Opg*$^{-/-}$ mice on the apolipoprotein E background were provided by M. Scatena (University of Washington). DOP is a well-characterized S1P lyase inhibitor that competes with the pyridoxal-5′-phosphate binding domain of the enzyme and causes peripheral lymphopenia[61]. It was administered to mice via drinking water at 30 mg/l (5 mg per kg body weight per day) or 3 mg/l (0.5 mg per kg body weight per day; OVX model) for the indicated times. iPTH (80 µg per kg body weight) and vehicle (NaCl) subcutaneous injections were performed daily for 5 d per week over 6 weeks. FTY720 was administered in drinking water (10 mg/L for a dose of 1.25 mg per kg body weight per d) for 7 weeks. Intraperitoneal calcein injection (30 mg per kg body weight) for assessment of dynamic bone formation was performed 9 d and 2 d before sacrifice. All procedures were approved by the Landesamt für Natur, Umwelt und Verbraucherschutz NRW, Germany.

µCT analysis. Quantitative microcomputed tomography of femura was performed using a SkyScan X-ray Microtomograph 1072 and CT Analyzer version 1.13.5.1 + (SkyScan, Belgium). Femur bones were placed in a tight-fitting plastic tube to prevent movement during scanning. For analysis of the femoral midshaft, a region 0.4 mm in length in the mid-diaphysis was analyzed. This region was then used to calculate diaphyseal parameters, such as cortical thickness and BMD. Image acquisition was performed at 100 kV and 98 µA with an angular increment of 0.45° between projections. Voxel size was 19 µm (isotropic). Density calibration was performed against hydroxyapatite phantoms with densities of 250 mg/cm^3 and 750 mg/cm^3. For the distal femoral metaphysis region, 800 transverse CT slices covering a region of 6.3 mm were acquired. Image acquisition was performed at 100 kV and 98 µA with an angular increment of 0.45° between projections. Voxel size was 8 µm (isotropic). Image reconstruction was done using NRecon software (version 1.6.9.4; SkyScan, Belgium), and appropriate corrections were applied. Trabecular bone was manually segmented from cortical bone and trabecular bone parameters were analyzed over 126 slices, starting 50 slices distal from growth plate. Analyses were performed in agreement with guidelines for assessment of bone microstructure in rodents using µCT[62].

Mechanical testing. A three-point bending test was performed until failure of the femura using a Material Testing System Shimadzu EZ Test EZ-SX device. Load and deflection curves were collected using TrapeziumX Software (Shimadzu, Kyoto, Japan). A support span of 5 mm at the bottom of the femura was used, and the load was applied at the midpoint of the posterior aspect of the femura. All tests were performed using a 500-N load cell at a constant loading rate of 3 mm/min. The data were collected every 5 ms. The ultimate force and stiffness were obtained directly from the load and deflection curves. The elastic modulus and ultimate stress were calculated using the following formulae: elastic modulus = $KL^3/(48\ I_{min})$; ultimate stress = $F_{ult}Lc/(4\ I_{min})$. K = stiffness; L = Gauge-length; I = moment of inertia; F_{ult} = ultimate force; Lc = bone radius.

Histology and histomorphometry. Cryosectioning was performed as previously described[63]. The left mouse femur was excised, and the distal part was snap-frozen in the embedding medium (C-EM001, Section Lab Co. Ltd., Kanagawa, Japan) using liquid nitrogen. 5-µm-thick cryosections were cut using a Leica CM 1850 cryotome, disposable stainless steel blade (Feather Microtome Blades, Type N35) and a cryosection preparation kit (C-EM001-C3, Section Lab Co. Ltd, Kanagawa, Japan) as described previously[64]. The cryofilm containing the bone sections was then glued onto a glass slide using 2% chitosan (Sigma) solution in 0.25% acetic acid, and the slides were stored at −80 °C until staining. On the day of staining, the bone cryosections were thawed at room temperature and allowed to air dry. Then, they were washed with 100% ethanol for 5 min to remove the embedding medium. This was followed with tissue fixation for 5 min in 4.5% formaldehyde (Roth, Roti Histofix). The sections were then stained for osteoid using a modified von Kossa staining method with McNeal's counterstain. Alkaline phosphatase histochemistry was performed according to a modified protocol by Miao and Scutt[64]. Shortly after, cryosections were air dried and placed in PBS with 0.2% Tween-20 for 10 min and then were rinsed in PBS for 10 min. The sections were incubated for 30 min at 37 °C in ALP substrate solution (100 mM Tris buffer, pH 9.2, containing 0.2 mg/ml Naphthol AS-MX phosphate dissolved in N,N-dimethylformamide and 0.4 mg/ml Fast Red TR), washed with distilled water and mounted with Faramount aqueous mounting medium. Masson Goldner and TRAP stainings were performed on methyl-methacrylate-embedded nondecalcified or decalcified femura and tibiae. Trabecular bone sections (7 µm) were obtained with a Leica RM2265 microtome (Leica Microsystems, Germany). Bone static histomorphometric analyses for OC.S/BS and OS/BS as well as bone dynamic histomorphometric analyses for MAR and BFR/BS were performed using Bioquant Osteo 2009 version 9.0 software (Bioquant Nashville, USA). At least two sections per mouse were analyzed by measuring the bone parameter specifically in the subepiphyseal region. Bone histomorphometric parameters were calculated according to the standardized nomenclature for bone histomorphometry[65]. Histological analysis of paraffin-embedded, H&E-stained WAT was performed by AxioVision40 version 4.8.2.0 (Zeiss). Cell size was calculated from two different slides with a quantification of at least three fields of view at 100-fold magnification.

Cell culture. MC3T3-E1 Subclone 4 was purchased from ATTC (CRL-2593). Primary OBs of long bones were isolated as previously described[66] with minor modifications. Briefly, long bones of mice aged 5–8 d were isolated and epiphyseal cartilage was removed and cut into 2 mm × 2 mm pieces that were placed on cell culture dishes, which were dried at 37 °C for 15 min before culture medium was added. Cells were cultured in DMEM (1 mg/ml glucose; Gibco) containing 10% FBS, 1 × antibiotic-antimycotic and 100 µM L-ascorbic acid-2-phosphate (Sigma). 3T3-L1 preadipocytes were obtained from the European Collection of Cell Culture (86052701, ECACC, Salisbury, UK). Differentiation was performed according to the supplier's instructions using 0.25 µM dexamethasone, 0.5 mM 3-Isobutyl-1-methylxanthine (IBMX) and 1 µg/ml insulin (Sigma). Supplementation with 1 µM S1P (Enzo) was performed daily, starting with induction of differentiation. JTE013 (Cayman) was added 30 min before S1P.

Cellular assays. *Oil Red O staining.* 3T3-L1 cells were seeded at 20,000 cells/cm^2, fixed with 4% neutral buffered formalin and stained with Oil Red O (Sigma). Lipid accumulation was quantified by Cy5 fluorescence intensity (Typhoon system, GE Healthcare). Calcium deposition was measured using a calcium reagent set (Teco Diagnostics). Cells were washed and lysed in 0.6 N HCl overnight at 4 °C. Supernatants were collected and calcium was measured at 575 nm and normalized to 1 mg protein per sample.

Western blot analysis. Nuclear extracts were prepared using hypotonic buffer (20 mM Hepes, pH 7.5, 5 mM sodium fluoride, 10 µM sodium molybdate, 0.1 M EDTA) followed by incubation on ice for 15 min and permeabilization by 10% NP-40 in ddH_2O. After centrifugation at 300 *g* for 30 s, the pellet containing the nuclear fraction was solubilized in RIPA and stored at −80 °C. Isolation of total protein after treatment with 1 µM S1P with or without preincubation with JTE013, TY52156 or SB203580 was performed in RIPA and followed with incubation on ice for 30 min. Cell lysates were clarified via centrifugation at 14,000 *g* at 4 °C for 10 min and were stored at −80 °C. Protein concentrations were determined using a Bradford protein assay (BioRad Protein Assay no. 500–0006; BioRad). 25 µg of total protein was run on SDS-PAGE, and proteins were then transferred to

polyvinylidene difluoride (PVDF) membranes. Western blotting was performed after blocking in 5% nonfat milk–PBS for 1 h before incubation with primary antibodies (β-catenin no. C19220, Transduction Laboratories; phosphorylated Akt^{Ser473} (p-Akt^{Ser473}) no. 8271, p-$GSK3\beta^{Ser9}$ no. 9336, p-$p38MAPK^{Thr180/Try182}$ no. 9211, p38MAPK no. 9212, Cell Signaling) at 4 °C overnight. Membranes were washed 4 times in PBS with 0.5% milk and 0.05% Tween-20 and exposed to secondary antibodies (peroxidase-labeled anti–mouse IgG (H + L) no. PI-2000 or anti–rabbit IgG (H + L) no. PI-1000, Vector). Signals were visualized using enhanced chemiluminesence solution (Amersham ECL Western Blotting Detection Reagents no. RPN2106; GE Healthcare) and were detected using ChemiDoc XRS + Imaging System (BioRad).

qPCR. Total RNA was isolated using Invi Trap Spin Cell RNA Mini Kit (Stratec molecular). Reverse transcription of 500 ng was performed by using RevertAid First Strand cDNA Synthesis Kit (Thermo Scientific). qPCR was performed using iQ Syber Green Supermix (BioRad) with 1 µl reverse transcriptase for 40 cycles of 95 °C for 10 s, 55 °C for 10 s and 72 °C for 30 s. Primers for *Opg*, *Bglap1*, *Pparg*, *Fabp4* and *Lpl* were from Qiagen. All others primer sequences (*Postn*, *Sparc* and *Col1a*, *Wnt5a*, *Lrp5*, *Osterix*, *Cebpa*, *Cd36* and *Adipsin*) were from https://pga.mgh.harvard.edu/primerbank/.

ELISA. Mouse Osteoprotergerin/TNFRSF11b DuoSet ELISA (R&D), Quantikine ELISA TRANC/RANKL (R&D), PYD ELISA (BlueGene) and Procollagen I C-terminal Propeptide ELISA (Cloud-Clone Corp.) were all performed according to the manufacturer's instructions. Cell culture supernatants of MC3T3-E1 and primary OBs were harvested after 24 h in the presence or absence of 1 µM S1P with or without JTE013, TY52156, SB203580, WIF-1 or BOX5 (added 30 min before S1P).

Lipid extraction. Lipid extraction from mouse feces was performed according to published protocols[67,68]. Briefly, feces were collected, and the total weight of the feces of every single mouse was measured. 1 mg of feces was powdered, mixed with saline and a 1:1 chloroform–methanol mix and centrifuged at 1,000 *g* for 10 min at room temperature. The liquid phase containing the extracted lipids was isolated in a new tube for the evaporation of the liquid. The weight of the lipid content was measured.

Magnetic resonance imaging. MRI data were recorded at a vertical Bruker AVANCE III 9.4-T wide-bore NMR spectrometer (Bruker, Rheinstetten, Germany) operated by ParaVision version 5.1. Images were acquired using the Bruker microimaging unit Micro2.5 with actively shielded gradient sets (1.5 T/m). Mice were anesthetized with 1.5% isoflurane in a water-saturated gas mixture of 20% oxygen in nitrogen, which was applied at a rate of 75 ml/min via manually restraining the mouse and placing its head in an in-house-built nose cone. Respiration was monitored by means of a pneumatic pillow positioned at the mouse's back. Vital function was acquired by a M1025 system (SA Instruments, Stony Brook, NY, USA) and used to synchronize data acquisition with respiratory motion for abdominal imaging. Throughout the experiments, mice were breathing spontaneously at a rate of approximately 100 breaths/min, and their body temperature was kept at 37 °C. Abdominal fat imaging was carried out using a 30-mm saw resonator essentially as described previously[69,70]. In brief, mice were placed within the resonator; in the *z*-direction (30 mm), the field of view (FOV) covered the abdomen from just below the diaphragm down to the pelvis. Abdominal fat content was determined via acquisition of axial images using 2D multislice turbo spin echo (TSE) sequences with and without fat suppression. Data were taken from a FOV of 25.6 × 25.6 mm^2 and a spatial resolution of 100 × 100 µ m^2 (TSE factor, 8; echo time (TE), 4.4 ms; repetition time (TR), 3,500 ms; slices, 30; slice thickness (ST), 1 mm; acquisition time (TAcq), 84 s). Using the same receiver gain, two image sets were recorded with and without chemical shift selective inversion recovery sequence for fat suppression. To produce essentially fat-only images, fat-suppressed data were subtracted in absolute intensity mode from nonsuppressed dataset through an in-house-developed software module based on the LabVIEW package (National Instruments, Austin, USA). For further analysis, all datasets (suppressed, nonsuppressed, fat-only) were imported into the 3D visualization software Amira (Mercury Computer Systems, Mérignac, France). With reference to the corresponding fat-suppressed anatomical images, signals in fat-only images were sectioned with constant threshold using the Segmentation Editor of Amira. For quantification of the fat content, the integral was calculated over the segmented area and related to the total volume analyzed as determined from the anatomical reference images.

Laboratory measurements of human blood samples. Venous blood samples were taken from the cubital vein of participants in the supine position. The sampling was performed between 7:00 a.m. and 2:00 p.m. with the majority of samples (97%) being taken in the mornings before 12 a.m. Serum aliquots were stored at −80 °C. Serum PTH, PINP and CTX concentrations were determined on the IDS-iSYS Multi-Discipline Automated Analyzer (Immunodiagnostic Systems Limited, Frankfurt am Main, Germany). For each analyte, three concentrations of control material were measured. Serum PTH concentrations were measured with the IDS-iSYS Intact PTH assay. The coefficients of variation were 16.8%, 10.7% and 9.0% at low, medium and high concentrations of control material, respectively. Serum PINP concentrations were measured with the IDS-iSYS Intact PINP assay. The coefficients of variation were 4.4%, 4.5% and 4.3% at low, medium and high concentrations of control material, respectively. Serum CTX concentrations were measured with the IDS-iSYS CTX-I (CrossLaps) assay. The coefficients of variation were 7.5%, 5.2% and 4.5% at low, medium and high concentrations of control material, respectively. Serum calcium concentrations were measured photometrically on the Dimension VISTA (Siemens Healthcare Diagnostics, Eschborn, Germany). Two concentrations of control material were measured, and the coefficients of variation were 2.9% and 4.2% at low and high concentrations of control material, respectively.

Determination of S1P concentration in human serum. S1P concentrations were measured using liquid chromatography–tandem mass spectrometry as previously described[71]. In brief, 20 µl of serum was incubated with 20 µl of the internal standard (1 µmol/L [16,17,18-2H7]-S1P (S1P-d7, Avanti Polar Lipids, Alabaster, AL, USA)). Subsequently, proteins were precipitated with 350 µl of acetonitrile/water (80/20, vol/vol). After centrifugation at 10,000 *g* for 15 min the extracts were subjected to reverse-phase chromatography on a Zorbax SB-C8 column (2.1 mm × 50 mm; Agilent Technologies, Santa Clara, CA, USA) at a flow rate of 0.35 ml/min. S1P was eluted with a binary gradient for 6 min (methanol/acetonitrile/0.1% formic acid, 2.5/2.5/95, vol/vol/vol to methanol/acetonitrile/0.1% formic acid, 30/30/40, vol/vol/vol) and measured via tandem mass spectrometry (Varian L1200 MS/MS, Agilent Technologies, Waldbronn, Germany) in the multiple reaction mode, monitoring the [M + H] + S1P parent ion ($m/z = 380$) fragmentation to the daughter ion ($m/z = 264$). The internal standard S1P-d7 with the m/z transition of 387 to 271 was used to correct for variations in sample preparation and instrument response. Calibration curves (four levels of S1P: 0, 0.1, 0.3, 1 and 3 µmol/L) were generated to calculate absolute S1P concentrations in serum samples.

Quantitative ultrasound measurement. In SHIP-trend participants, QUS measurements were performed at the heel using the Achilles InSight device (GE Medical Systems Ultrasound, GE Healthcare, Chalfont St Giles, UK), a water-based bone ultrasonometer, as described previously[72]. The measurements were performed successively on both feet of seated participants by trained and certified examiners. Alcohol was used as coupling agent. The system measures the frequency-dependent attenuation of the sound waves (broadband ultrasound attenuation, BUA) and the speed of sound waves (SOS) as they pass through the heel (os calcis). BUA and SOS were combined to form the Stiffness index according to the following formula: stiffness index = (0.67 × BUA) + (0.28 × SOS) − 420.

Statistical analysis. *SHIP-trend statistics.* Continuous data are expressed as median (1st–3rd quartile), and categorical data are expressed as proportions. Group comparisons were performed using the Chi-squared or Kruskal–Wallis test. $P < 0.05$ was considered statistically significant. The relation between BMI and S1P was assessed in a linear regression model adjusting for age and sex. A curvilinear association was found and was modeled with restricted cubic splines with three knots located at the 5th, 50th and 95th percentile, as recommended[73]. BMI, besides age and sex, was thus considered as a confounder in the linear regression analyses assessing the relations between stiffness index, PTH, calcium, PINP, CTX and S1P. Additionally, adjusted mean S1P concentrations with 95% confidence intervals according to the QUS-based fracture risk were calculated with a one-way ANOVA. In all models, sex was tested as a potential effect modifier, but no significant interactions were detectable. Sex-specific data are presented in the Supplementary Information. All statistical analyses were performed with SAS 9.4 (SAS Institute Inc., Cary, North Carolina, USA).

Other statistical analysis. The statistical significance of differences between groups was evaluated using a paired or nonpaired two-tailed *t*-test or a one-way ANOVA with Tukey's multiple-comparisons test (GraphPad Prism 5.0; GraphPad Software, La Jolla, CA, USA). Data were tested for normality and equal variance before analysis. All results are expressed as mean ± s.e.m. Detailed statistical information for all the data presented in this study is listed in Supplementary Table 3.

Reporting Summary. Further information on experimental design is available in the Nature Research Reporting Summary linked to this article.

Data availability. The data that support the findings of this study are available from the corresponding author upon reasonable request. Uncropped immunoblot images are available in Supplementary Fig. 12.

References

61. Schwab, S. R. et al. Lymphocyte sequestration through S1P lyase inhibition and disruption of S1P gradients. *Science* **309**, 1735–1739 (2005).
62. Bouxsein, M. L. et al. Guidelines for assessment of bone microstructure in rodents using micro-computed tomography. *J. Bone Miner. Res.* **25**, 1468–1486 (2010).

63. Kawamoto, T. & Kawamoto, K. Preparation of thin frozen sections from nonfixed and undecalcified hard tissues using Kawamot's film method (2012). *Methods Mol. Biol.* **1130**, 149–164 (2014).
64. Miao, D. & Scutt, A. Histochemical localization of alkaline phosphatase activity in decalcified bone and cartilage. *J. Histochem. Cytochem.* **50**, 333–340 (2002).
65. Dempster, D. W. et al. Standardized nomenclature, symbols, and units for bone histomorphometry: a 2012 update of the report of the ASBMR Histomorphometry Nomenclature Committee. *J. Bone Miner. Res.* **28**, 2–17 (2013).
66. Declercq, H. et al. Isolation, proliferation and differentiation of osteoblastic cells to study cell/biomaterial interactions: comparison of different isolation techniques and source. *Biomaterials* **25**, 757–768 (2004).
67. Kraus, D. et al. Nicotinamide N-methyltransferase knockdown protects against diet-induced obesity. *Nature* **508**, 258–262 (2014).
68. Kumar, A. et al. Profile of clients tested HIV positive in a voluntary counseling and testing center of a district hospital, Udupi, South Kannada. *Indian J. Community Med.* **33**, 156–159 (2008).
69. Burghoff, S. et al. Deletion of CD73 promotes dyslipidemia and intramyocellular lipid accumulation in muscle of mice. *Arch. Physiol. Biochem.* **119**, 39–51 (2013).
70. Tucci, S., Flögel, U., Sturm, M., Borsch, E. & Spiekerkoetter, U. Disrupted fat distribution and composition due to medium-chain triglycerides in mice with a beta-oxidation defect. *Am. J. Clin. Nutr.* **94**, 439–449 (2011).
71. Moritz, E. et al. Reference intervals for serum sphingosine-1-phosphate in the population-based Study of Health in Pomerania. *Clin. Chim. Acta* **468**, 25–31 (2017).
72. Schürer, C. et al. Fracture risk and risk factors for osteoporosis. *Dtsch. Arztebl. Int.* **112**, 365–371 (2015).
73. Stone, C. J. & Koo, C. Y. Additive splines in statistics. in *Statistical Computing Section, Proceedings of the American Statistical Association* 45–48 (American Statistical Association, Washington, DC, 1985).

nature research

Corresponding author(s): Bodo Levkau

☐ Initial submission ☐ Revised version ☒ Final submission

Life Sciences Reporting Summary

Nature Research wishes to improve the reproducibility of the work that we publish. This form is intended for publication with all accepted life science papers and provides structure for consistency and transparency in reporting. Every life science submission will use this form; some list items might not apply to an individual manuscript, but all fields must be completed for clarity.

For further information on the points included in this form, see Reporting Life Sciences Research. For further information on Nature Research policies, including our data availability policy, see Authors & Referees and the Editorial Policy Checklist.

Experimental design

1. Sample size

Describe how sample size was determined.

Sample size was based on previous studies with the same treatments and genotypes but other readouts or were based on pilot studies in which statistically significant differences were observed. In ovariectomy experiments, power calculations for sample size were based on expected iPTH effects on bone and approved by the National animal care committee, the 'Landesamt für Natur, Umwelt und Verbraucherschutz Nordrhein-Westfalen', Germany.

2. Data exclusions

Describe any data exclusions.

No samples or animals were excluded

3. Replication

Describe whether the experimental findings were reliably reproduced.

All attempts for replication were successfull

4. Randomization

Describe how samples/organisms/participants were allocated into experimental groups.

Random allocation into experimental groups.

5. Blinding

Describe whether the investigators were blinded to group allocation during data collection and/or analysis.

Investigators were blinded to group allocation during data collection and analysis.

Note: all studies involving animals and/or human research participants must disclose whether blinding and randomization were used.

6. Statistical parameters

For all figures and tables that use statistical methods, confirm that the following items are present in relevant figure legends (or in the Methods section if additional space is needed).

n/a	Confirmed
☐	☒ The exact sample size (*n*) for each experimental group/condition, given as a discrete number and unit of measurement (animals, litters, cultures, etc.)
☐	☒ A description of how samples were collected, noting whether measurements were taken from distinct samples or whether the same sample was measured repeatedly
☐	☒ A statement indicating how many times each experiment was replicated
☐	☒ The statistical test(s) used and whether they are one- or two-sided (note: only common tests should be described solely by name; more complex techniques should be described in the Methods section)
☐	☒ A description of any assumptions or corrections, such as an adjustment for multiple comparisons
☐	☒ The test results (e.g. *P* values) given as exact values whenever possible and with confidence intervals noted
☐	☒ A clear description of statistics including central tendency (e.g. median, mean) and variation (e.g. standard deviation, interquartile range)
☐	☒ Clearly defined error bars

See the web collection on statistics for biologists for further resources and guidance.

Software

Policy information about availability of computer code

7. Software

Describe the software used to analyze the data in this study.	SAS 9.4, SAS Institute Inc., Cary, North Carolina, USA; GraphPad PRISM for MAC 6.0, GraphPad Prism 5.0, GraphPad Software, La Jolla, CA, USA; LabVIEW package, National Instruments, Austin, USA; Amira, Mercury Computer Systems, Mérignac, France; ParaVision 5.1, Bruker, Rheinstetten, Germany; TrapeziumX Software, Shimadzu, Kyoto, Japan; Bioquant Osteo 2009 V9.0, Bioquant Nashville, USA; AxioVs40 V4.8.2.0, Carl Zeiss, Germany; Skyscan x-ray microtomograph and CT Analyzer version 1.13.5.1+, Skyscan, Belgium.

For manuscripts utilizing custom algorithms or software that are central to the paper but not yet described in the published literature, software must be made available to editors and reviewers upon request. We strongly encourage code deposition in a community repository (e.g. GitHub). *Nature Methods* guidance for providing algorithms and software for publication provides further information on this topic.

Materials and reagents

Policy information about availability of materials

8. Materials availability

Indicate whether there are restrictions on availability of unique materials or if these materials are only available for distribution by a for-profit company.	No restrictions apply.

9. Antibodies

Describe the antibodies used and how they were validated for use in the system under study (i.e. assay and species).	Western blot primary antibodies (Beta-catenin #C19220, Transduction Laboratories; p-Akt Ser473 #8271, p-GSK3beta Ser9 #9336, p38 MAPK Thr180/Try182 #9211, all Cell Signaling; p38 MAPK #sc-535; Santa Cruz). For ELISA studies, DueSet mouse Osteoprotergerin/TNFRSF11b ELISA (R&D), Quantikine ELISA TRANC/RANKL (R&D), PYD ELISA (BlueGene) and Procollagen I C-Terminal Propeptide ELISA (Cloud-Clone Corp.) were used. The manufacturer has either stated that cross-reactivity to mouse is guaranteed and provided appropriate controls or cells/tissues recommended by the manufacturer but not supplied have been acquired and employed as controls.

10. Eukaryotic cell lines

a. State the source of each eukaryotic cell line used.	MC3T3-E1 Subclone 4 was purchased by ATTC® (CRL2593™). 3T3-L1 preadipocytes were from the European Collection of Cell Culture (86052701, ECACC, Salisbury, UK).
b. Describe the method of cell line authentication used.	Cells were purchased directly from ATCC and ECACC. All parameters were in accordance to product information provided by the supplier and the literature.
c. Report whether the cell lines were tested for mycoplasma contamination.	No testing performed as cells were freshly from supplier.
d. If any of the cell lines used are listed in the database of commonly misidentified cell lines maintained by ICLAC, provide a scientific rationale for their use.	No listing.

Animals and human research participants

Policy information about studies involving animals; when reporting animal research, follow the ARRIVE guidelines

11. Description of research animals

Provide details on animals and/or animal-derived materials used in the study.	Both sexes of each mouse strain were used with exact numbers and ages provided for each experiment. Regular and ovariectomized C57Bl6J mice were form Charles River Laboratories. S1P2-/- mice were kindly provided by Jerold Chun, Scripps Research Institute, inducible S1P lyase knockout mice by Andreas Billich, Novartis, and OPG-/- mice on the apolipoprotein E background by Marta Scatena, University of Washington.

Policy information about studies involving human research participants

12. Description of human research participants

Describe the covariate-relevant population characteristics of the human research participants.

Human data were obtained from the SHIP-TREND cohort study, which is the second independent population-based cohort of the Study of Health in Pomerania (SHIP). A number of n=4,096 individuals are included in this study with a median age of 52 years (1st - 3rd quartile: 40-64 years); 51.9% women. A detailed descriptive statistics of the study population is enclosed with the manuscript. There are 276 studies in the literature published with the SHIP study (current PubMed search 9/10/2017). For reference: Volzke, H., et al. Cohort profile: the study of health in Pomerania. Int J Epidemiol 40, 294-307 (2011).

nature research

Corresponding author(s): Bodo Levkau

☐ Initial submission ☐ Revised version ☒ Final submission

MRI Studies Reporting Summary

Form fields will expand as needed. Please do not leave fields blank.

Experimental design

1. Describe the experimental design.	Determination of abdominal fat
2. Specify the number of blocks, trials or experimental units per session and/or subject, and specify the length of each trial or block (if trials are blocked) and interval between trials.	Two experimental blocks per subject, 40 min per block, one day interval
3. Describe how behavioral performance was measured.	N/A

Acquisition

4. Imaging	
a. Specify the type(s) of imaging.	Morphological, fat and water quantification
b. Specify the field strength (in Tesla).	9.4 T
c. Provide the essential sequence imaging parameters.	Turbo spin echo, chemical shift selective imaging, FOV 30x30 mm2, matrix 256x256, axial or sagittal slice orientation, slice thickness 0.5-1 mm, TR 3500 ms, TE 4.5 ms
d. For diffusion MRI, provide full details of imaging parameters.	N/A
5. State area of acquisition.	Abdomen, calf

Preprocessing

6. Describe the software used for preprocessing.	ParaVision 5.1 (Bruker)
7. Normalization	
a. If data were normalized/standardized, describe the approach(es).	N/A
b. Describe the template used for normalization/ transformation.	N/A
8. Describe your procedure for artifact and structured noise removal.	Respiratory gating
9. Define your software and/or method and criteria for volume censoring, and state the extent of such censoring.	N/A

Statistical modeling & inference

10. Define your model type and settings.	N/A
11. Specify the precise effect tested.	Differences in tissue fat and water content, respectively

12. Analysis

a. Specify whether analysis is whole brain or ROI-based. ROI-based

b. If ROI-based, describe how anatomical locations were determined. Manual segmentation

13. State the statistic type for inference. (See Eklund et al. 2016.) ANOVA

14. Describe the type of correction and how it is obtained for multiple comparisons. N/A

15. Connectivity

a. For functional and/or effective connectivity, report the measures of dependence used and the model details. N/A

b. For graph analysis, report the dependent variable and functional connectivity measure. N/A

16. For multivariate modeling and predictive analysis, specify independent variables, features extraction and dimension reduction, model, training and evaluation metrics. N/A